UNIVERSITY OF CALIFORNIA SAN DIEGO

Detection and Estimation of Moisture in Hybrid Perovskite Photovoltaic Films

A Thesis submitted in partial satisfaction of the requirements
for the degree of Master of Science

in

Materials Science and Engineering

by

Shreya Rengarajan

Committee in charge:

Professor David P. Fenning, Chair
Professor Javier Garay
Professor Sheng Xu

2021

The thesis of Shreya Rengarajan is approved, and it is acceptable in quality and form for publication on microfilm and electronically.

University of California San Diego

2021

TABLE OF CONTENTS

LIST OF FIGURES

LIST OF TABLES

ACKNOWLEDGEMENTS

I would like to express my gratitude to Prof. David Fenning for guiding me through this entire journey. I have always respected you for being a brilliant professor, but over the past year, working for you has made me realize how valuable your mentorship has been. Thank you for giving me this wonderful opportunity and being a positive reinforcement throughout. I also want to thank Rishi for introducing me to Python coding and literally being with me every step of my project. Moses, you have taught me all the nitty-gritty of film fabrication and I can say for a fact that I have learnt from the best and thank you for it. I would also like to extend my thanks to rest of the SOLEIL group for being great mentors and wonderful colleagues.

I would like to thank my family who have been the source of my strength while pursuing graduate school. In a foreign country halfway across from my home, regular video calls with you - Mom, Dad and Prathu, have made me feel like you have been right next to me this whole time. Thank you for always having faith in me.

Finally, I want to thank all my friends for being pillars of support, through grad school and covid. Thanks to Sid for helping me with Python coding – I will not be the brilliant coder that I am today, had it not been for all those pip installations that you helped me through a year ago! To my other friends in SD – La Regencia roomies, Sid, Satchit and Jeb, thanks for making sure grad school does not mean being socially dead. A special mention to Apoorva, Ranjith, Adithan and Swami for those check-in calls to make sure each of us were still well and sane. I hope we finally manage to make our 734th plan to meet up stick!

ABSTRACT OF THE THESIS

Detection and Estimation of Moisture in Hybrid Perovskite Photovoltaic Films

by

Shreya Rengarajan

Master of Science in Materials Science and Engineering

University of California San Diego, 2021

Professor David P. Fenning, Chair

With the focus of global energy production shifting towards renewables, efforts have been made to develop sustainable, low-cost technologies to cater to our needs while protecting our environment. The past decade has seen an exponential increase in the popularity of perovskite based solar cells with a push towards commercialization mainly due to its low processing cost, tunability and high efficiency. Despite the attractive advantages offered by perovskite solar cells, one of its shortcomings is its long-term stability. The research community has been invested in tackling issues related to understanding this water-perovskite interaction which poses a threat to

device stability. It is known that moisture is one of the most challenging factors to tackle when it comes to degradation of these devices. The presence of water has a detrimental impact on the film's composition, structure as well as optical properties. Thus, monitoring the uptake of water without destroying the nature of the film altogether is extremely crucial since it directly translates to optimization of the levelized cost of energy efficiency.

Researchers have extensively studied the effects of this complex interaction, but there has not been an attempt to isolate the presence of moisture in these films in order to study the cause itself - Water. This thesis aims to study the interaction between water and perovskites using an in-situ and non-destructive technique based on the short-wave infrared (SWIR) spectroscopy.

CHAPTER 1: Introduction

1.1 Global Energy Outlook and Climate Change

On our planet today, we have roughly 7.8 billion people and this number is projected to be steadily increasing at ~1% each year [1]. Each grown human being consumes 115.7 W of energy to sustain our bodies [2]. In addition to the bare minimum required for our sustenance, we use energy for a myriad of things in our daily lives. On an average, the global energy consumption in 2018 has been estimated to be 600 quadrillion Btu (in the order of 10^{15}!) according to the U.S. Energy Information Agency[3]. Every activity which adds carbon dioxide to the atmosphere will proportionally determine the extent of global warming. The demand for per capita energy requirement will always show an upward trend, bolstered by several factors such as technological developments and increase in living standards, all of which have a potential chance of increasing global carbon footprint. This challenges us to come up with a creative solution to tackle our ever-growing energy demands while seeking to achieve net zero or negative carbon emissions.

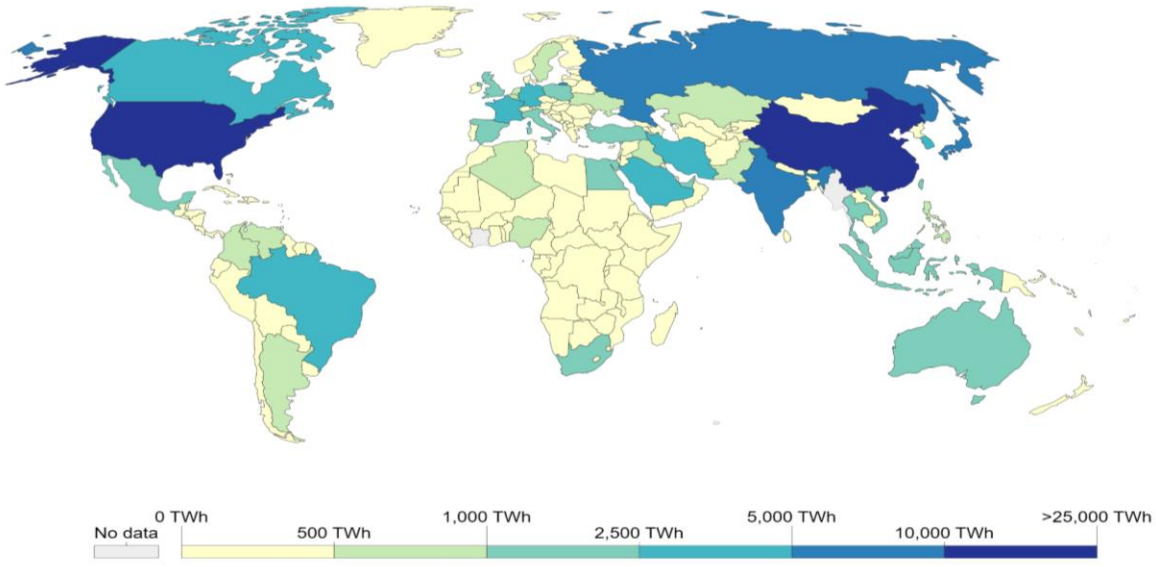

Figure 1.1: Global primary energy consumption in 2019, measured in terawatt-hours (TWh)[4]

Figure 1.1 gives us a rough idea of how primary energy consumption is distributed across the world[4]. Primary energy consumption refers to a combination of total energy consumption including electricity, transport and heating [4]. In countries such as the U.S.A which falls under a higher bracket of energy consumption, one of the major contributing factors would be industrialization and higher living standards in contrast to the population in some developing countries such as China and India. Per capita consumption paints a better picture in that aspect in pinpointing the distribution of energy consumption across the world. Countries such as Iceland, Norway, Canada, the United States and some of the middle east countries such as Bahrain, Saudi Arabia and Qatar are among the highest energy consumers in the world[4]. The challenge of reducing carbon footprint is not as easy as it seems because of the disparity in the global energy consumption based on the region. The development of technologies which can control carbon emissions in energy sector largely done by the usage of green energy sources – especially wind and solar energy which is expected to show an increasing trend according to the EIA[3]. With advancements in science and technology, there has been a huge growth in the renewable energy sector which has led to an overall decrease in the carbon footprint since usage of coal and natural gas electric generation which had a combined share of 63% in 2018 fell to 59% in 2020 and is predicted to drop to 58% in 2021[3].

1.2 Growth in Renewable Energy and Solar PV

Renewable energy carriers are energy sources which are replenished by natural processes at a rate comparable or faster than its rate of consumption [2]. The use of these alternative fuels has made headway to clean and sustainable development practices. Sustainable development requires methods and tools to measure and compare the environmental impacts of human activities for

various products. Adopting these principles, the use of renewable energy contributes to zero or almost zero emissions of greenhouse gases and air pollutants [5]. These systems can also be deployed in a modular manner, making it flexible to the demands of that region. There are various forms of renewable energy carriers - Solar fuels, Hydroelectricity, Wind Energy, Bio Energy, Geothermal energy etc. Figure 1.2 shows the growth in each of sectors over the last couple of years.

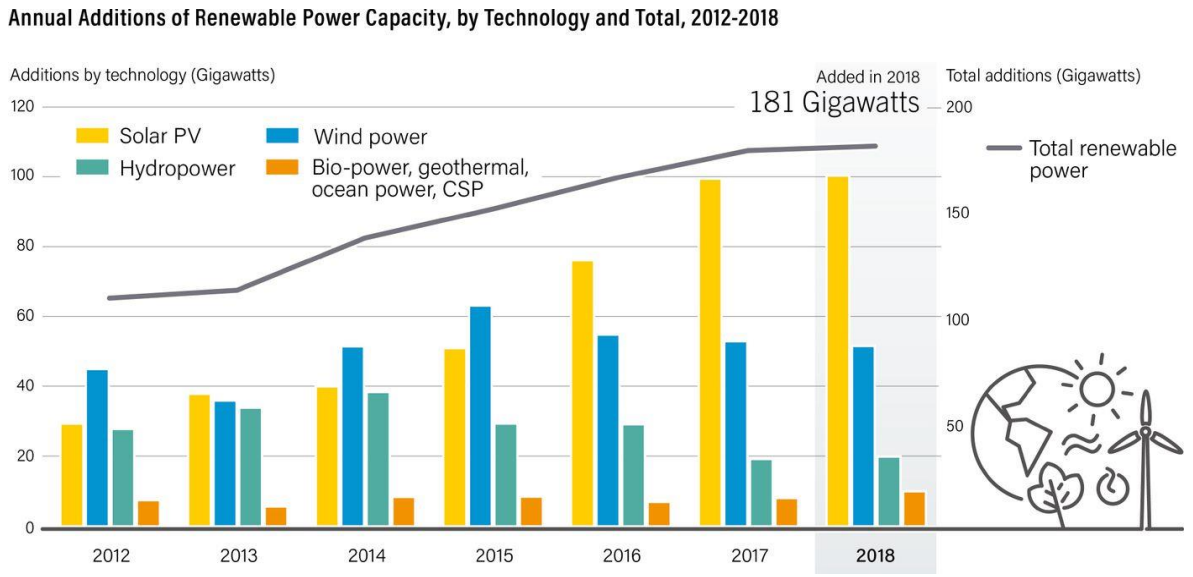

Figure 1.2: Growth in renewable energy sector over the last decade[5]

The chart shows a steady growth in the use of renewables, dominated by solar photovoltaics. The Sun is an abundant source of energy - it emits a total of 3.8×10^{23} kW of energy out of which 1.8×10^{14} kW gets through to the Earth, making it a promising source of energy[5]. Solar energy can be harnessed either as thermal energy or can be converted into electricity. The direct conversion of solar energy into electricity is done using photovoltaic devices. These devices make use of semiconducting materials to harness sunlight. The dominant technology which has been in the PV market has been based on Silicon arrays, panels and cells. These systems ideally have a lifetime of over 20 years and require minimal maintenance post installation[6]. Over the last two decades, researchers have been working on finding alternative processes and/or materials for

solar PV. The growth in the domain of solar PV is orchestrated by the trifecta of the cost factor, efficiency factor and the stability factor. Extensive research has gone into background engineering of solar cells which is needed in order to maximize efficiency and stability while minimizing the cost per module. This would subsequently lower the device LCOE (levelized cost of energy), thereby making it economically viable for large scale manufacturing. One such alternative material which has been quick to gain popularity is perovskite based solar cells.

1.3 Perovskite Solar Cells

Solar cells are electronic devices which convert sunlight into electricity directly using the principle of photovoltaic effect. This process requires the use of a photoactive material - one where the material raises its electrons into active state on being excited by a light source. These generated electrons dissipate the absorbed energy in an external circuit in the form of electricity before returning to the absorber [10]. There are three major steps which describes the working principle of a solar cell, which are -

1. Charge excitation: Absorption of photons from the sun to produce “free” electrons.
2. Charge separation: Separate the generated electrons and holes to increase the device lifetime and prevent recombination.
3. Charge collection: Extraction of the charge carriers (electrons and holes) into an external circuit in order to generate current.

The performance of a solar cell is governed by several factors, including its power conversion efficiency (PCE). Like energy conversion efficiency, a solar cell’s PCE is defined by the proportion of incident power which is converted into electricity.

Perovskites are a class of materials with a general formula of ABX_3 (X = oxygen, carbon, nitrogen or halogen). The crystal structure of a hybrid organic-inorganic perovskite, methylammonium lead iodide ($CH_3NH_3PbI_3$) is shown in Figure 1.3. The A site cation in this case is $CH_3NH_3^+$ which occupies the cubo-octahedral site, and the B site cation is Pb^{2+}, in an octahedral site. The anion, I^- is present in the edge-center position, thereby satisfying the charge neutrality [7].

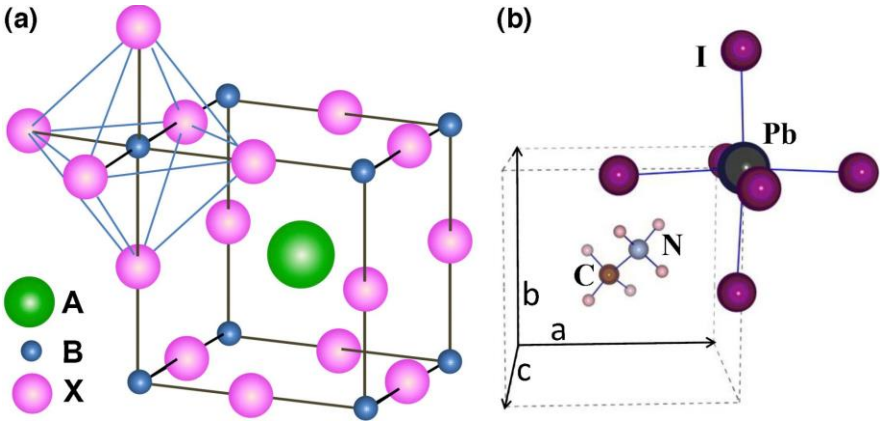

Figure 1.3: (a) ABX_3 crystal structure along with a BX_6 octahedral (b) A single unit cell of cubic phase $CH_3NH_3PbI_3$[7]

The stability and distortion of this crystal structure is heavily dependent on its geometry - often decided by a dimensionless variable, Goldschmidt tolerance factor (t). It is calculated using: $t = \frac{r_A + r_X}{\sqrt{2}(r_B + r_X)}$ where r_A, r_B, r_X refers to the effective ionic radius for A, B and X, respectively. For an ideal cubic perovskite structure, t must be equal to 1 and for values less than 1, the crystal structure will have some octahedral distortions. Although the tolerance factor is not the only predictor of perovskite crystal structure, the formability of a perovskite will not be affected if the tolerance factor is within the appropriate range ($0.813 < t < 1.107$) [7]. Perovskite solar cells use these perovskite structured materials such as methylammonium lead iodide (abbreviated as $MAPbI_3$), formamidine lead iodide ($FAPbI_3$) etc., as the absorber layer.

1.3.1 Evolution of perovskites in PV

The research in the field of perovskites has come a long way from a mere 2.2% efficiency reported by Miyasaka and co-workers back in 2006 to a 25.5% as of today [8,9].

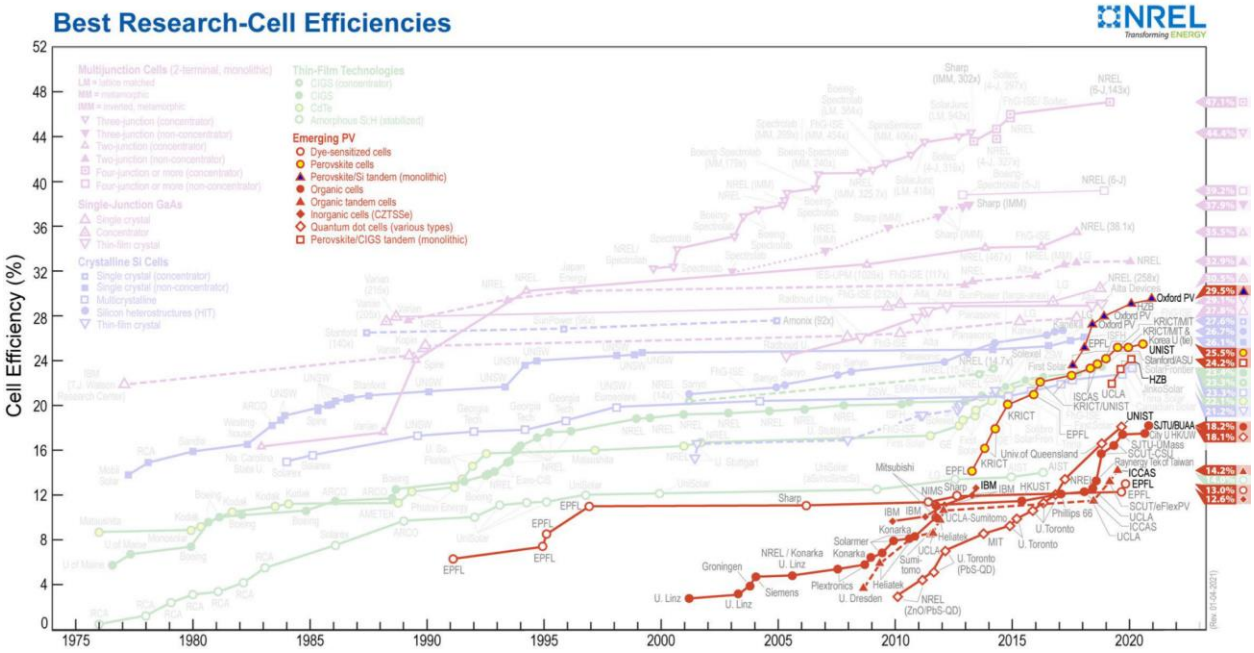

Figure 1.4: Growth in R&D of emerging PV technologies[9]

The device architecture has undergone major evolution in its usage in these photovoltaic cells. The perovskites were initially used as a sensitizer material in Gratzel's dye-sensitized solid-state cells. The initial architecture had the hole transporting material (HTM) completely infiltrated into a mesoporous oxide layer, thereby forming a heterojunction. The later architectures proved that sensitization is not a requirement for a good cell design and the electron transport system can be supported by the perovskite layer itself. Hence, after significant research on identifying a better suited HTM, researchers have adopted for a planar heterojunction pin/nip concept[7]. There is a shortfall for pin devices in efficiencies which is compensated by its stability.

1.3.2 Why do perovskites make good optoelectronic materials?

Perovskites make for an excellent choice of absorber or active layer in a solar cell architecture. These can be attributed to a variety of reasons which has made it so popular over the last two decades.

1. Strong optical absorption: Perovskites exhibit a strong absorption across the UV-vis wavelength region. They have large absorption coefficient, wide absorption window, moderate exciton diffusion length and excellent charge-carrier mobility [11]. $MAPbI_3$ has an absorption onset at 790nm (corresponds to a bandgap Eg = 1.5 eV). Owing to the broad absorption window which overlaps with solar spectral irradiance, perovskites can successfully harvest photons thereby maximizing the photocurrent in the device [11].

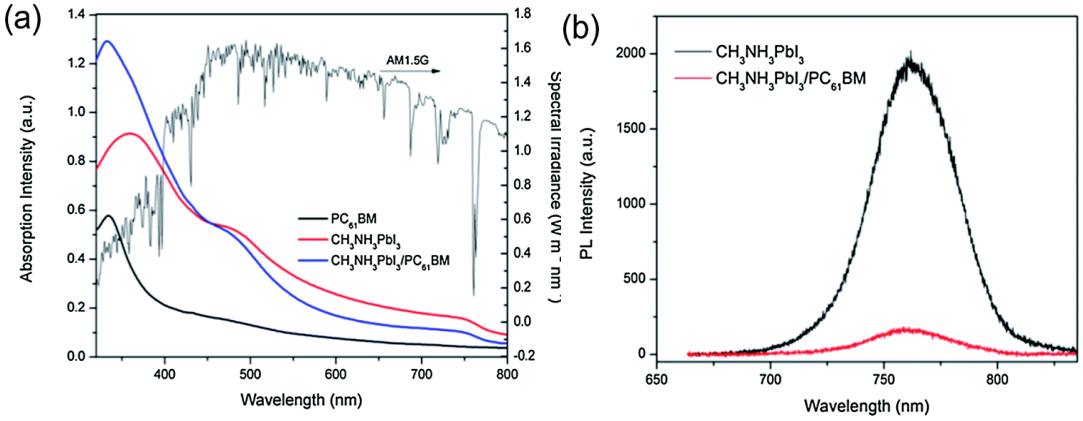

Figure 1.5: UV-vis absorption spectra of $MAPbI_3$ and $MAPbI_3$/HTM bilayer superposed over the AM 1.5G solar spectrum (b) Steady state PL spectra [11]

2. Low non-radiative recombination rates and defect tolerance: This property enables perovskites to have relatively low values for difference between open circuit voltage (V_{oc}) and effective bandgap potential (E_g/q) as well as have relatively high external radiative efficiency. This allows for use of perovskites as a top cell (with high E_g) in a tandem device architecture [8].

Shallow level defects (donors and acceptors) are responsible for doping in a solar cell. The presence of defects at deeper energy levels causes non-radiative recombination in a cell, thereby decreasing its V_{oc}. In perovskites ($MAPbI_3$) researchers have found that deep state defects have high formation energy, because of which dominant point defects only generate at shallow levels [12].

3. Tunable bandgap: Hybrid organic-inorganic perovskites are versatile in nature, allowing for an ability to tune its optoelectronic property by changing their chemistry. In $MAPbI_3$, the iodine can be replaced with other halogens such as chlorine and bromine, $MAPbCl_3$ and $MAPbBr_3$ with a bandgap of 1.53 eV, 2.97 eV and 2.24 eV for the I, Cl and Br perovskite, respectively. Similarly, the monovalent cation can also be substituted - MA can be replaced with formamidinium ion ($CH(NH_2)_2^+$ or FA) [13]. The A site cation also allows for mixed substitution of multiple ions (MA/FA/Cs) in a particular ratio.

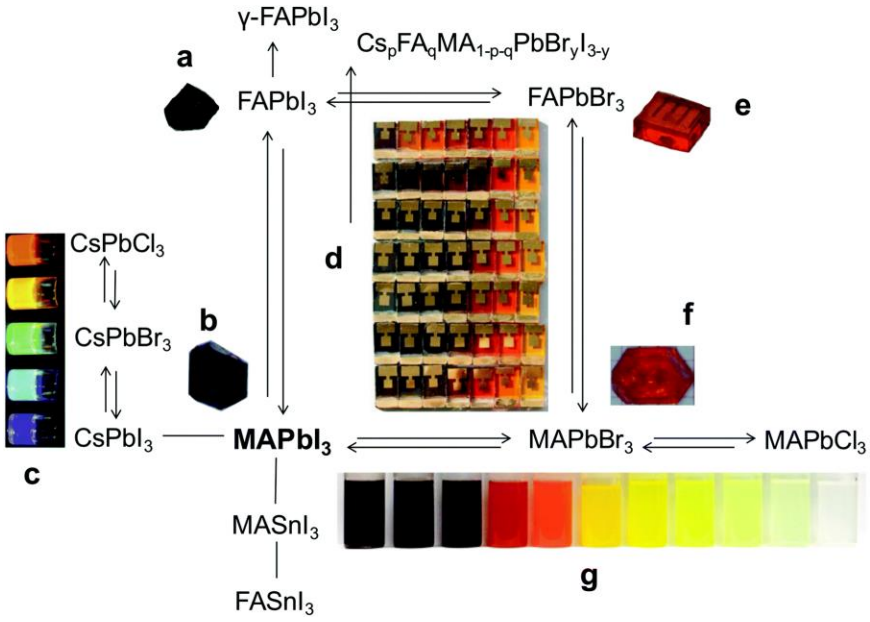

Figure 1.6: (a), (b), (e) and (f) are single crystals of $FAPbI_3$, $MAPbI_3$, $FAPbBr_3$ and $MAPbBr_3$ (c.), (g) colloidal solution of $CsPbX_3$ and $MAPbX_3$; (d) solar cells made with various compositions in MA/FA Pb Br/I [13].

4. Large bulk collection length: Perovskites have long electron-hole diffusion lengths which exceed the film thickness[12]. This maximizes the charge carrier collection before recombination could occur.

In addition to possessing excellent optoelectronic properties, perovskites have low processing cost combined with an ease of production. This makes the technology extremely economical to scale up, making it one of the most attractive alternatives when it comes to commercialization.

1.3.3 Challenges in commercialization

Among emerging PV technologies though perovskites are surely a forerunner with a competitive edge, there are still a few challenges which need to be addressed in order for it to dominate the market. Primarily, the stability of the film is of concern. Perovskites are susceptible to various forms of degradation in contrast to silicon which has rock-like stability, allowing it to last for over 25 years. When it comes to perovskites, water plays a critical role in being one of the major detrimental factors in its degradation [7,8,14]. There have been several steps that have been taken to remedy this situation, including extensive encapsulation of these modules to prevent moisture ingress. Some of the other proposed solutions include changes in stoichiometry and compositional tuning to make the thin film more robust. A concern based on consumer perception in commercialization of this technology is the use of toxic Pb in the device composition. Researchers have been working on substitution of other elements for Pb, in order to make it more environmentally friendly [7].

1.4 Motivation and scope of thesis

With the focus of global energy production shifting towards renewable energy production, efforts have been made to develop sustainable, low-cost technologies to cater to our needs while protecting our environment. Perovskite solar cells have been an attractive emerging PV technology which almost matches the efficiency of Silicon PV while providing a processing and cost advantage. This competitive edge is determined by the estimation of the levelized cost of energy of the solar cell module, which also takes into account the long-term stability of a module in addition to the processing cost. Despite the attractive advantages offered by perovskite solar cells, one of its shortcomings is its long-term stability. The research community has been invested in tackling issues related to understanding this water-perovskite interaction which poses a threat to device stability, since commercialization would involve its deployment outdoors. As a step towards improving the robustness of the device, it is essential to understand the phenomenon of moisture-perovskite interactions. The presence of water has a detrimental impact on the film's composition, structure as well as optical properties. Thus, monitoring the uptake of water without destroying the nature of the film altogether is crucial since it directly translates to an increase in the levelized cost of energy efficiency.

This thesis aims to study the interaction between water and perovskites using an in situ and non-destructive technique based on the short-wave infrared (SWIR) spectroscopy. There is extensive literature on the effects of this complex water-perovskite interaction, but there has not been an attempt to isolate the presence of water in these films in order to study the cause in itself - Water. Water Reflectometry Detection (WaRD) is a successfully validated technique which has previously been employed to study and quantify moisture in silicon solar modules [15]. WaRD

utilizes SWIR to map the water content in a solar cell and can estimate the uptake which occurs in films. Unlike silicon, perovskite thin films have a rather complicated composition and crystal structure. While conducting this study using WaRD spectroscopy, the presence of organics and inorganics will have to be dissociated and the process of studying the uptake must be deconvoluted in order to pick up water's spectroscopic signature. Using scientific concepts and tight process controls, this work examines the ingress of water, establishes detection technique, eliminates possible extraneous sources of error and develops a technique to study the effect of water in an organic-inorganic triple cation perovskite film via a non-invasive approach.

CHAPTER 2: Interaction of Water in Perovskites

2.1 Moisture and solar cells

There are different ways in which moisture ingress occurs in a solar module. In a silicon PV module, water is known to diffuse into the cells through their breathable back sheets or the encapsulant polymers such as ethylene vinyl acetate (EVA) sheets which have rather high diffusivity [18]. Once moisture gets into the polymer, it slowly penetrates to reach the solar cell thereby weakening the interfacial adhesive bonds which results in the delamination of the module. The increase in the number of ingress pathways causes loss in passivation and corrosion of the metallic contacts [18,19]. For a perovskite solar module, the ingress of water occurs directly in the perovskite layer chemistry, unlike silicon. The presence of water leads to deprotonation of the methylammonium cation to produce methylamine, hydrogen iodide and lead iodide as degradation products [20]. Solar cell deployment is outdoors, where they are exposed to hot and humid environmental conditions. Since moisture hence plays a detrimental role in leading to PV module failure and must be tightly controlled.

Moisture ingress can be prevented in a silicon module by use of a true hermetic seal or changing the encapsulant material to make it impervious to moisture by selecting one with low diffusivity or by incorporating desiccant properties in the encapsulation. For a perovskite solar cell, in addition to device encapsulation there are other proposed methods to prevent or minimise moisture ingress. The choice of a hydrophobic hole transport material (HTM) or device passivation which could be carried out by using hydrophobic polymer material are among the proposed methods to restrict ingress of water [20].

2.2 Absorption spectrum of water

Pure water has a broad and complex absorption range across the entire electromagnetic spectrum, particularly in the infrared region. This spectrum is obtained due to vibrations of water molecules which differ with the incident energy. In the far infrared (IR) region, the absorption of water occurs through intermolecular vibrations. In the IR region, the absorption is via intermolecular vibrational transitions and moving towards the ultraviolet (UV) region, the electronic transitions lead to water absorption.

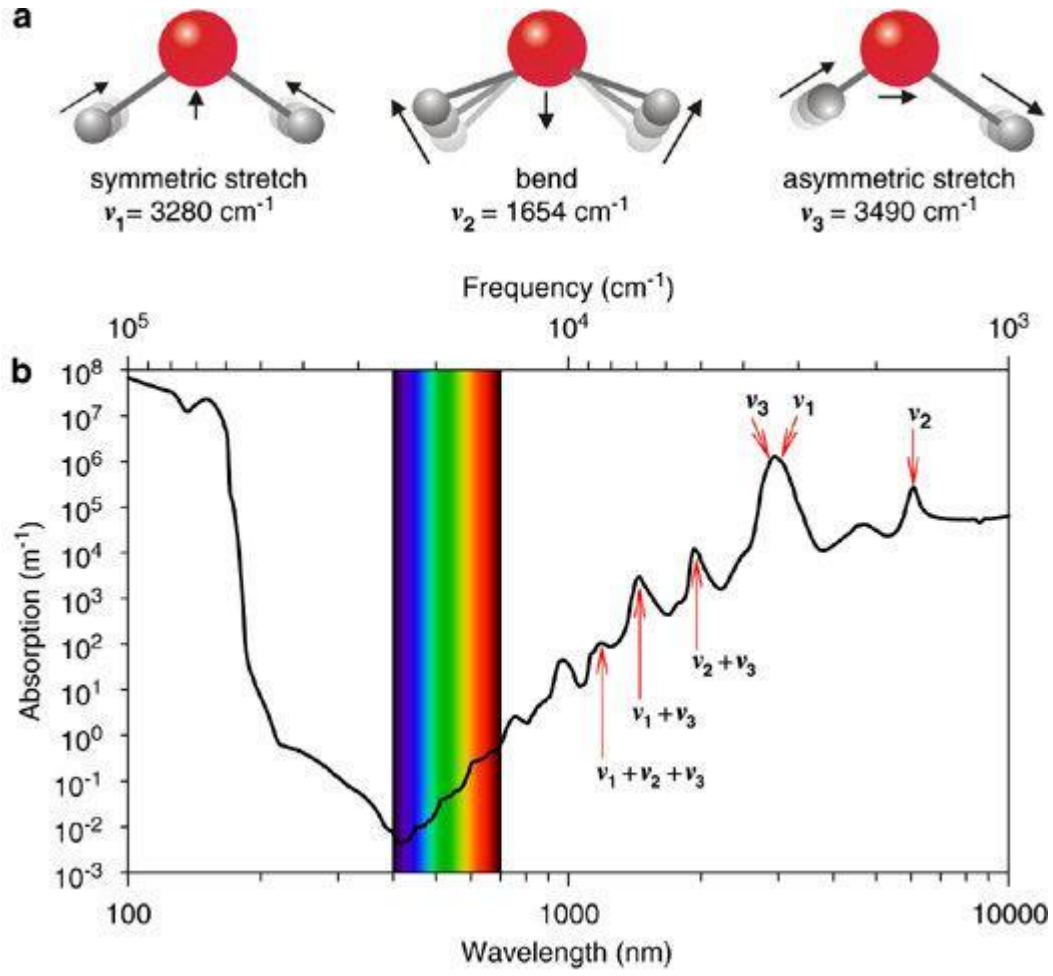

Figure 2.1: (a) Three vibrational modes of water (b) Absorption spectrum with fundamental and harmonics [22]

Water absorption, as mentioned earlier, is an effect of various vibrational modes of water. These can be broadly classified into fundamental and overtones (combinational) bands. There are

three fundamental vibrational modes of water - $\boldsymbol{\nu}_1$ is the symmetric stretching of the oxygen molecules with respect to the hydrogen, $\boldsymbol{\nu}_2$ is the bending mode and $\boldsymbol{\nu}_3$ is the asymmetric stretching of O with respect to H molecule. In the N-IR window of observation, there are two main peaks of water which are of interest. They are the 1450 nm and 1900 nm wavelength peaks which are comprised of overtones: $\boldsymbol{\nu}_1 + \boldsymbol{\nu}_3$, $2\boldsymbol{\nu}_3$, $2\boldsymbol{\nu}_2 + \boldsymbol{\nu}_3$ (for 1450 nm) and $\boldsymbol{\nu}_2 + \boldsymbol{\nu}_3$ (for 1902 nm) respectively [23]. The reason for choosing to study overtones is because these peaks are easier to resolve and they are more responsive to any changes in external temperature, solute addition or changes in atmospheric water content. This "response" is due to changes in the hydrogen bond strength [21].

2.2.1 Deconvoluting water peaks in NIR region

Water has spectroscopic signature across the electromagnetic spectrum, but predominantly, in the NIR region the two overtones of water occurring at 1450 nm (6900 cm^{-1}) and 1900 nm (5200 cm^{-1}) are studied since they display characteristic shift towards higher or lower wavelengths when the hydrogen bond strength gets increased or decreased respectively. For example, when the temperature is increased, the strength of the H bond decreases, thereby shifting the water peaks towards lower wavelengths. The water band is well-defined at 5200 cm^{-1} as compared to the 6900 cm^{-1} band since there is little to no overlap with the N-H overtone bands from the perovskite film composition [21].

2.2.2 1450 nm pure water band

Previous literature studies have shown that the 1450 nm band, which is due to the combination of symmetric and antisymmetric stretching of O-H modes, experiences a peak shift range of nearly 40nm when the sample is subjected to a temperature change from 6℃ to 80℃.

The NIR water spectra results studied by Segtnan et al have been obtained by 2D NIR correlation spectroscopy and principal component analysis [24]. The reason for this peak shift which occurs with temperature is due to weakening of the intermolecular hydrogen bonds, as discussed earlier. This H bond weakening strengthens the covalent O-H bond. There is an interplay between the bending and stretching vibrations with temperature. The stretching band peak lowers in intensity and tends to shift to higher frequencies (lower wavelength) as a result of an increase in temperature, whereas the bending band peak becomes narrower and more stronger and hence would tend to shift to lower frequencies (higher wavelength) with an increase in temperature. When it comes to the 1450nm (6900 cm^{-1}) band, there is a dominance of the stretching band over the bending band, therefore shifting the peaks to a lower wavelength as depicted in Figure 2.2 [24]. The spectra when consolidated gives an isosbestic point at 1446 nm. Isosbestic refers to the point at which the total absorbance does not change with the occurring chemical reaction that is aimed at causing a change in the first place.

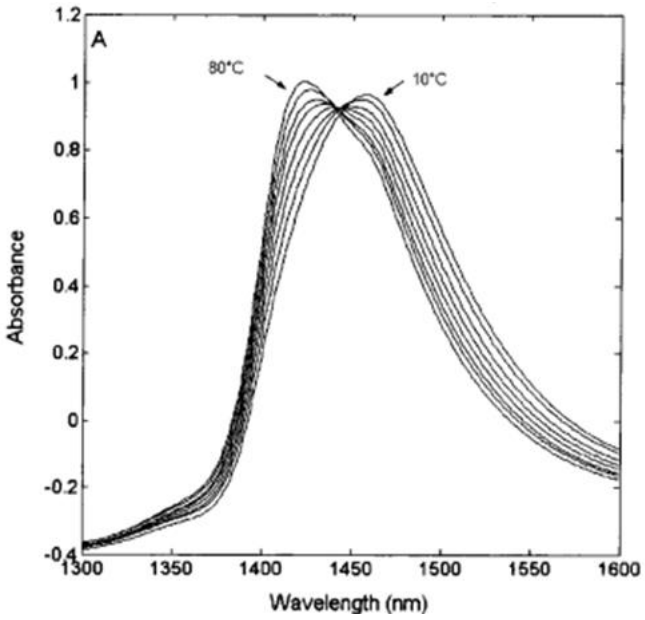

Figure 2.2: NIR spectra showing a blueshift in water peak with increasing temperature [24]

2.2.3 1940 nm pure water band

The water peak at 1900 nm (5200 cm^{-1}) is a combinational band consisting of the $\boldsymbol{\nu}_2 + \boldsymbol{\nu}_3$ vibrational or bend-stretch bands. These have less overlap with N-H bond vibrations and would shift to higher wavenumber with reduced hydrogen bond strength, like the other N-IR water peaks. A shoulder of the 1.94 μm absorption band is found at 1.8 μm which accounts for the lower absorption coefficient (α) in this region [25]. The difference is seen in terms of a much sharper and larger absorption coefficient than some of the other overtones. The exact peak position is dependent on several factors such as the measurement temperature, the environment of testing (for instance, the presence of 1900 nm water peaks in a perovskite chemistry would be significantly different from the same peak as observed in a solution of tetrachloromethane (TCM) [26].

Table 2.1 N-IR pure water absorption peaks and their absorption coefficients (cm^{-1}) [25]

Wavelength (μm)	Water path length (cm)	Spectrometer band width (μm)	Wavelength of max absorption	Abs coeff at max absorption (cm^{-1})
1.35 - 1.80	0.090	0.003	1.45	26.0
1.80 - 2.50	0.022	0.004	1.94	114.0

2.3 Water-Perovskite interaction

It is a well-known fact that perovskite halides are sensitive to moisture and this interaction is still one of the unresolved bottlenecks when it comes to commercialization of these devices. The presence of water in perovskite films impacts various aspects of the crystal structure as well as the film. Figure 2.3 enlists some changes which occur as a result of this interaction.

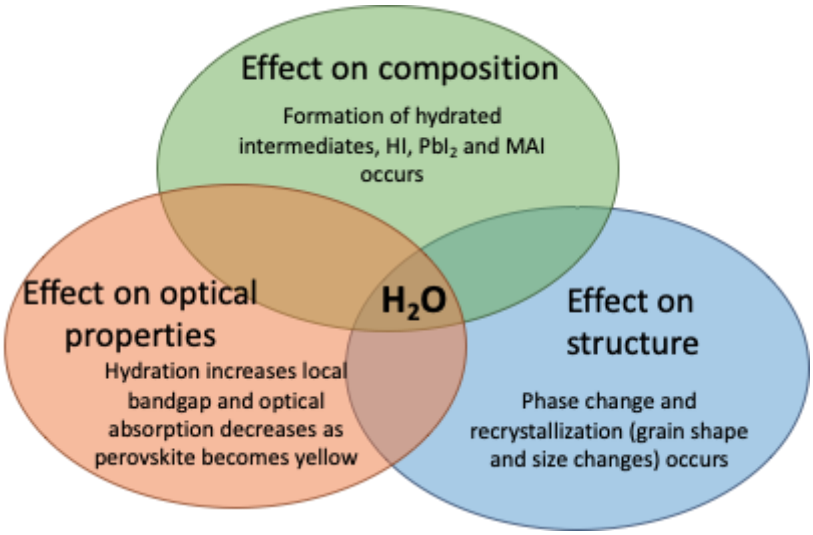

Figure 2.3: Effects occurring due to moisture-perovskite interaction.

2.3.1 Effect of H_2O on perovskite composition

Water acts as a catalyst and changes the chemical composition of the perovskite film. Controlled exposure of water in air causes degradation of these films which occurs due to chemical degradation involving the catalyst role of water. Under vacuum, the proposed degradation mechanism is through thermodynamic degradation by creation of volatile molecular defects [28]. The degradation in itself is a two step process where as a first step, the hydrated crystal phase (monohydrate) is formed as soon as perovskites get exposed to water vapor. This phase change is fully reversed when the material is subsequently dried [27]. Prolonged exposure leads to the formation of the dihydrate which ends with an irreversible reaction leading to the formation of the dihydrate along with PbI_2 and excess H_2O.

$$4\,(CH_3NH_3)PbI_3 \;+\; 4\,H_2O \;\Leftrightarrow\; 4[CH_3NH_3PbI_3\,.H_2O] \;\rightarrow$$

$$(CH_3NH_3)_4PbI_6\,.2H_2O \;+3\,PbI_2 \;+\; 2\,H_2O$$

The hydration process of perovskite is isotropic and homogeneous on a macroscopic scale, although phase separation occurs on a microscopic scale [27]. PbI_2 formation on degradation occurs in the bulk due to fast diffusion of water as well as organic cations. The presence of lead iodide

affects the device's long term photostability. This decomposition rate of perovskite film is related to the exposure to the degree of relative humidity. It has been shown that on exposure to relative humidity greater than ~50%, $MAPbI_3$ devices show rapid detrimental consequences on their performance [27]. Studies have shown that dry N_2 or low humid air encourages the back reaction of perovskite hydration proving that the monohydrate is a reversible reaction [28].

2.3.2 Effect of H_2O on perovskite structure

H_2O affects the perovskite structure by causing phase changes and distortion of grain shape and sizes. The initial ingression of water is found to chemisorb on a particular region of $MAPbI_3$, extracting the n-type charge carriers from the surface, just like how a p-type dopant would. At high humidity, water tends to restructure the crystal structure by causing surface hydration, leading to polycrystalline structures and grain boundaries [28]. Water has negative binding energy in the region of MA^+ near the edges. The more negative the binding energy, it makes it favorable. Ingress occurs from the edges. These intercalated water molecules are found to increase lattice constant of $MAPbI_3$ (by nearly 6%), causing an increase in lattice distortion and band gap [30]. The hydration kinetics involve - high degree of penetration of moisture, and diffusion of water molecules along grain boundaries.

2.3.3 Effect of H_2O on optical properties

When H_2O molecules are chemisorbed on the surface of the film, they behave similar to the p-type dopants, so this shifts the valence band maximum (VBM) as well as the conduction band maximum (CBM) to lower values [31]. Since chemisorbed water molecules interact only electrostatically with the perovskite instead of chemically, they do not affect the bandgap (E_g) by

a lot. The presence of water improves the local E_g of MAI^- very slightly because of the shift in CBM, but the E_g of PbI_2 increases by ~0.3eV [28]. But once H_2O molecules permeate into the inner space, the local band gap increases from ~1.6 eV to 3.1 eV (hydrated perovskite) and finally settles at 2.4 eV (PbI_2) on complete degradation [32]. Perovskite films undergo color change from dark brown to yellow on continuous exposure to water which can be observed with naked eyes. Along with this color change, the optical absorption of the film also decreases.

2.3.4 Fundamentals of water bonding in $MAPbI_3$ perovskite

Water binds differently with different species of the perovskite chemistry, some groups being energetically more favorable than others [33]. There are three different kinds of bonds which water can form -

1. H_2O-MA^+ bond: The bond between water and the organic group is called the hydrogen bond, but the strength of it is determined by the presence of an extra hole from the net positive charge, making the hydrogens more "proton-like". The H_2O molecule also transfers some charge to MA^+, arising due to some covalency and orbital mixing. This site is energetically favorable and becomes a triaxial water bonding environment without causing any disruption to the $MAPbI_3$ inorganic network. Naturally, this binding mode has the most negative binding energy of $E_{binding}$ (H_2O) = -0.60 eV [33].
2. H_2O-PbI_3^- bond: The Pb^{2+} cations sit right at the center of an PbI_6 octahedron, causing a symmetric distribution of negative charges around the positive center. This prevents natural bond formation between H_2O and Pb^{2+}, and hence would occur only if Pb^{2+} is pushed off-center. This bond formation requires water-induced distortion which is symmetry-

breaking, making it a high energy bonding and thereby least favorable with a binding energy of $E_{binding}$ (H_2O) = -0.22 eV [33].

3. H_2O-$MAPbI_3$ bond: As discussed above, there are two distinct water binding sites, (a) H-MA^+ interaction and (b) distortion of an octahedron to interact with exposed Pb^{2+}. On average, water's interaction with $MAPbI_3$ is significantly lower in energy than its bonding with Pb^{2+}, making it a more favorable choice. In this case the octahedral distortion is not as much and MA^+ still is a triaxial boding site. The binding energy is $E_{binding}$ (H_2O) = -0.42 eV [33].

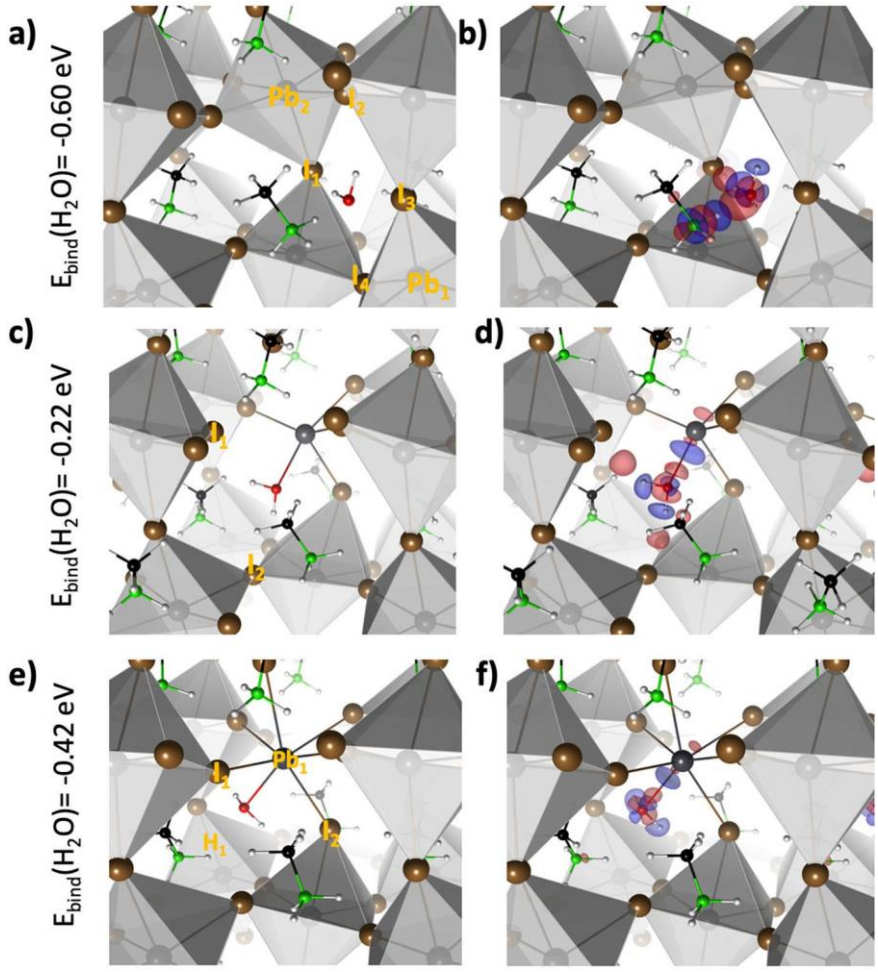

Figure 2.4: Different modes of binding of H_2O in a 0.25 H_2O:MA concentration of $MAPbI_3$ chemistry (a) - (b) H_2O-MA^+ bond (c.) - (d) H_2O-PbI_3- bond and (e) - (f) H_2O-$MAPbI_3$ bond [33]

2.3.5 Water in perovskite fabrication: An upside!

We have seen how susceptible to moisture perovskite films are and all of the detrimental effects that H_2O has on the properties of the film. But there have been literature reports which claim a positive effect that water has on the formation of perovskite films which ultimately lead to an improvement in its photovoltaic performance! [37] Triple cation perovskites [$Cs_{0.05}(FA_{0.83}MA_{0.17})_{0.95}Pb(I_{0.83}Br_{0.17})_3$ abbreviated as Cs/FA/MA] is fabricated per the usual solution processing procedure, with just one extra step of introducing 0-5% volume ratio of water to the Cs/FA/MA solution before spin-coating. Results indicate that the addition of moderate amounts of water (2% by volume) led to an enhancement in PCE from 18.1% to 19.4% because of recrystallization of the perovskite films which produces more crystalline films [37]. It is only the presence of bulk water which causes degradation of perovskites, whereas introduction of hydrate water leads to fabrication of high-quality films and devices.

2.4 Quantitative determination of moisture

Having understood various effects of water, it is imperative to detect the presence of water in the films. Based on literature, there have been several tests which can determine the water content which are not just pertaining to usage in perovskite films. These include:

- Carrier gas based coulometric barrier measurement
- Calcium test
- Cobalt chloride test
- Transmission based measurement techniques (FTIR spectroscopy and IR transmission measurements)
- Raman spectroscopy

Each of the tests mentioned above have their own limitations to pass as a successful field test. The carrier gas test lacks any spatial resolution, Ca test and the cobalt chloride test both are difficult to handle since it needs to be deposited before encapsulation and would cause damage to the property of the film tested [36]. The transmission-based measurements are limited in its usage on only the test films or modules. Raman spectroscopy allows for detection of water in degraded areas but cannot quantify the amount of water present in the film/module.

Using short-wave infrared (SWIR) reflection-based spectroscopy capitalizes on the two distinct water absorption bands in the near IR region which occurs as a result of combination of fundamental vibrations. Previously used to measure the amount of water in silicon modules, this technique has proven to be successful in isolation of water peaks [35]. In the N-IR wavelength range, all components of a silicon solar module are optically transparent, thereby providing a clear window of observation.

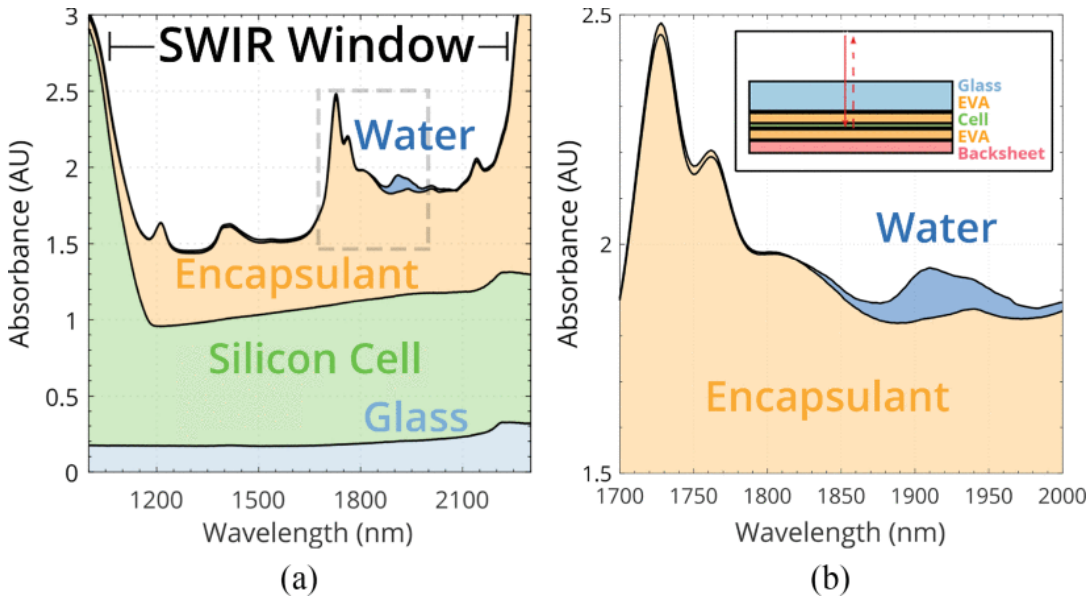

Figure 2.5: (a) Absorbance of PV module in the NIR wavelength (b) SWIR absorbance of water in an EVA-encapsulated PERC module[35]

CHAPTER 3: Experimental Methods

3.1 Theory and Setup of Water Reflectometry Detection (WaRD) Technique

Water has a broad range of absorption across the electromagnetic spectrum. In the infrared (IR) region, the absorption of water occurs through intermolecular vibrational transitions occurring due to a linear combination of lower energy modes. WaRD uses the short-wave infrared (SWIR) reflectometry to quantitatively determine the water content [15]. This SWIR window of observation consists of the two overtones of O-H vibrations which occur near 1450 nm (6900 cm^{-1}) and 1902 nm (5200 cm^{-1}) respectively, as seen in Fig 3.1 [16]. These overtones are "responsive" to changes in temperature and water concentration due to change in their hydrogen bond strength. This can be used to quantify the amount of moisture ingress.

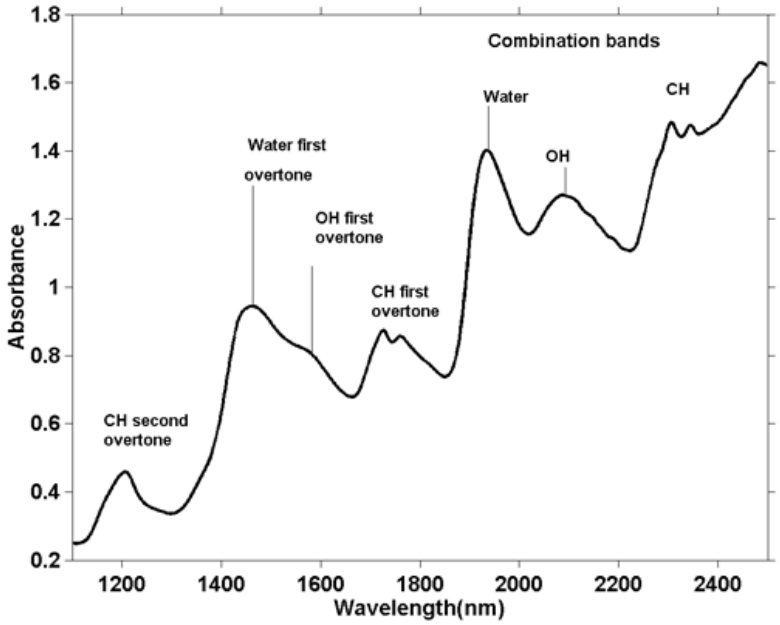

Figure 3.1: Absorption spectra including various vibrational bands in the near-IR region[16]

SWIR has been used to quantify moisture in various other fields such as characterization of biological molecules, soil etc. and it could be extended to detection of water in perovskites as

well. Neither the film nor the substrate exhibits any spectral changes in the N-IR spectroscopic signature of water, thereby allowing a clear window for us to make our observations. The WaRD setup capitalizes on this window in its front-side module reflectance measurement.

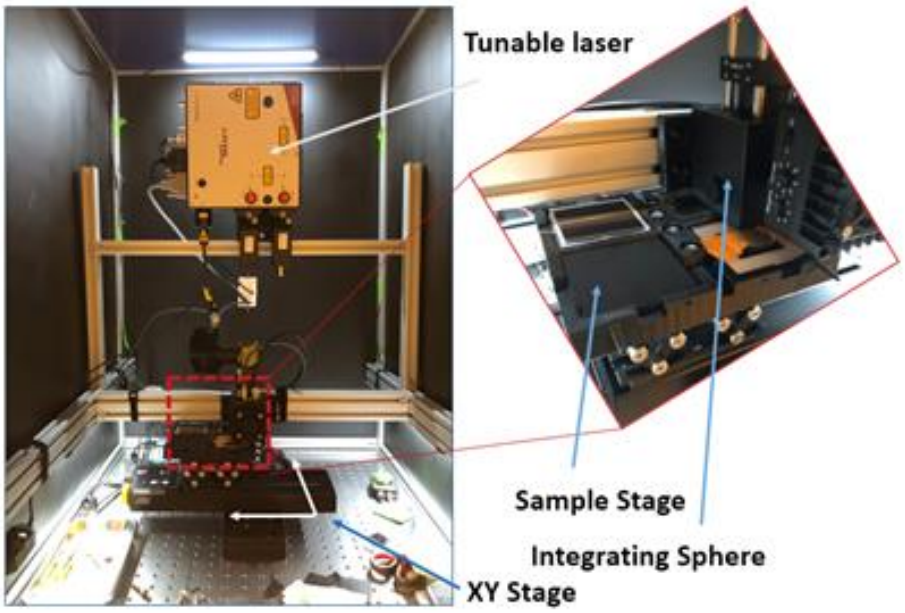

Figure 3.2: WaRD setup inside the optical cabinet

The setup, as shown in figure 3.2, uses a NKT SuperK COMPACT white light source tunable laser operating in the NIR regime to carry out the measurements. The total power output is > 110 mW delivered as an unpolarized input pulse trigger operating at 100-240V and 50-60 Hz. The detection is done using SR830 DSP lock-in amplifier operating at a sensitivity of 5 mV/nA and an integrating sphere which uses spectralon®, a diffuse reflectance standard which are the most lambertian reflector material. The stage bars (XY Stage) allow for movement in the x and y direction while the sample stage moves in the z direction to allow for tuning of the optical path. The films to be tested are placed under the laser in its optical path and the film reflectance is measured using the integrating sphere.

The reflectance values are then converted into absorbance data using beer's law - $A = -log(R) = \alpha * c * l_{path}$ where α is the absorption coefficient of the perovskite film at a particular wavelength, c is the concentration of moisture and $l_{path}$is the optical path length traversed by the laser.

3.2 Construction of in-situ RH chamber

Achieving a higher degree of control over the testing conditions is highly crucial for this study. Perovskites are extremely sensitive to even the slightest change in moisture content. In order to set up a controlled testing environment, a dual air-flow tunable humidity chamber was designed, the schematic of which is shown in Fig 3.3.

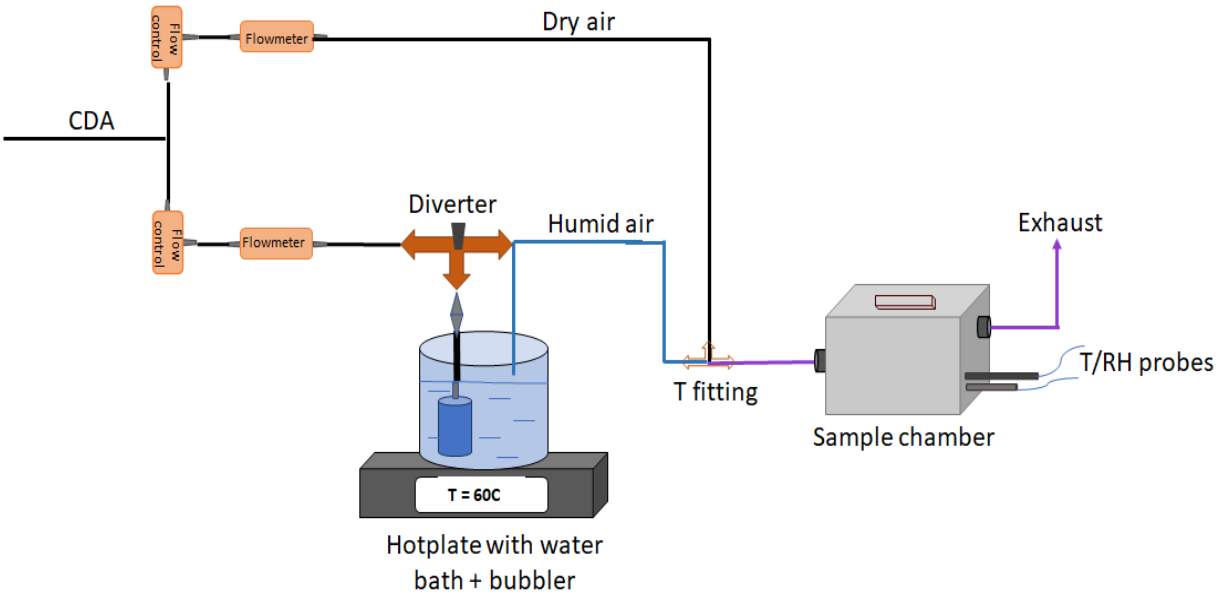

Figure 3.3: In-situ tunable humidity chamber schematic

This setup splits the main compressed dry air (CDA) into two different lines, one for humid air and the other is for dry air. Both these lines are controlled using a flowmeter. The humid air is generated by passing one of the CDA lines through a water bath-bubbler setup placed over a

hotplate, which allows for an increase in the achievable % relative humidity (RH) range. Both these lines are mixed and let into the sample chamber thereby allowing for a precise control of %RH inside the sample chamber by maintaining a fixed ratio of constant air flow. The design specifications of the in-situ RH chamber are detailed in Table 3.1.

Table 3.1 In-situ chamber design specifications

Design/control specification		**Description**
%RH range achievable		~ 5% to ~92%
Response/purge time		Under a minute (~45 seconds)
Flow rate (from CDA pressure regulator)		1.2 LPM - 3 LPM
Controls	*Temperature control*	- Hotplate to monitor temperature of water bath - Polyimide heating coil to control the temperature of the sample chamber
	Flow control	- Pressure regulator to control CDA flow upstream - Flowmeters controlling the flow of humid and dry air
Sensors	*RH sensor*	Humidity sensor placed inside the sample chamber to give an in-situ feedback of the %RH subjected to the films
	Temperature sensor	Temperature sensor to gauge the temperature of the air inside the sample chamber

The regulator used for flow control is an adjustable relieving regulator made of aluminum, with a maximum flow-rate of 53 scfm at 100psi with an accuracy of ±3%. A tunable variable area mechanical flowmeter is used to modulate the amount of dry and humid air that goes into the

sample chamber which is an aluminum corrosion resistant washdown enclosure of the dimensions $2\ 5/8$" x $2\ 5/8$" x $1\ 5/8$" (height x width x depth).

3.3 Sample preparation

3.3.1 Substrate preparation

Microscopic glass substrates were used for fabrication of the perovskite films. 25mm x 20mm films were cut and the substrates were thoroughly cleaned through a series of sonication baths. The procedure is as follows:

- 10 minutes sonification in 2% (by volume) Hellmanex glass cleaning solution in DI water
- 10 minutes sonification in isopropanol
- 10 minutes sonification in acetone

The substrates were then blow dried and plasma treated for 10 minutes on maximum power before perovskite solution processing.

3.3.2 Perovskite solution preparation

The perovskite film composition consists of the kitchen sink recipe consisting of triple cation with mixed halide of composition - Cs/FA/MA Pb $(Br/I)_3$ $[Cs_{0.05}(FA_{0.83}MA_{0.17})_{0.95}Pb(I_{0.83}Br_{0.17})_3]$ The fabrication of the film is solution-based processing using the spin coating method. The triple cation perovskite solution is put together by mixing $FAPbI_3$ and $MAPbBr_3$ in a 5:1 ratio with a 5% (by volume) addition of CsI solution. $FAPbI_3$ has a good bandgap but the active phase is thermodynamically unstable at temperatures below 150°C. In order to improve its stability, $MAPbBr_3$ is added. This addition also helps improve the device performance. Inorganic CsI addition further increases the film durability. $FAPbI_3$ and $MAPbBr_3$

solutions are made by mixing the weighed-out precursor powders (FAI + PbI_2 and MABr + $PbBr_2$ respectively) with solvents DMF and DMSO in the ratio of 4:1. The solutions prepared are 9% lead excess. Molarity checks are performed in the intermediate stages to make sure the nominal densities (1.5M) of the inorganic solutions are maintained. The CsI solution preparation involves mixing the appropriately weighed out amount of CsI with DMSO and heating the solution at 150°C until all the powder has dissolved. Once all precursor powders are added, the vial is treated on a vortex mixer to make sure that the powders have been completely dissolved into the solution of the triple cation perovskite. The substrates are plasma treated at maximum power for 10 minutes before perovskite deposition occurs. This renders it hydrophilic to the deposition.

3.3.3 Perovskite film fabrication and Au deposition

The fabrication process is done via a two-step spin coating deposition process, which is then followed by 45 minutes anneal at 115°C. The deposition itself takes 30 seconds per film with the first step at 1000 rpm (acceleration of 200 rpm/s) for 10 seconds and the second step at 5500 rpm (acceleration of 2000 rpm/s) for 20 seconds. 70 µL of the prepared perovskite solution is doctor-bladed onto the substrate in order to fully cover it. 12 seconds before the end of step 2 of the spin, dispense 250 µL of chlorobenzene anti-solvent in the center of the film. Once the spin process is complete, place the film over a preheated hotplate for annealing [18]. Thermal evaporation of gold was done over the entire face of the perovskite film. The deposition was carried out at a constant rate of 0.1 Å/s in a ramp mode process to give a 80nm thick Au layer over the perovskite.

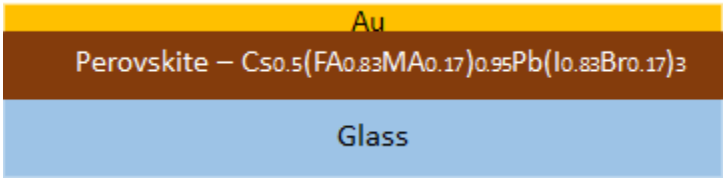

Figure 3.4: Cross section of the film used for WaRD testing.

3.3.4 Perovskite film encapsulation

Encapsulation of perovskite stack is effectuated by hot-pressing the sample to a glass cover by means of a polyisobutylene (PIB) rubber tape. The PIB tape is arranged in a desired pattern over the perovskite film and a glass cover is carefully placed over the film/PIB exposed side and gently pressed in place. This stack is then placed over a preheated hotplate set at 200°C with the glass cover in contact with the plate in order to minimize the heat faced by the perovskite film. Three preheated metal blocks are balanced over the film so as to distribute the pressure evenly across the film. The hot-pressing is done at about 20 psi for 15 minutes by which the PIB seal is evenly sealed without the presence of air bubbles. The encapsulation patterns used for various experiments are shown in figure 3.5.

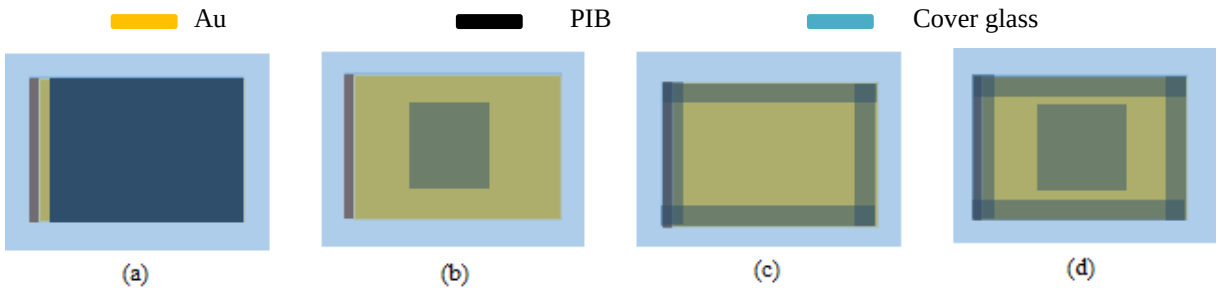

Figure 3.5: (a) Encapsulated with edge opening, (b) Square encapsulated, (c) Edge seal, (d) Square and edge seal

3.4 Experiments conducted

A series of experiments were carried out in order to isolate the water peaks and detect its presence in the triple cation $[Cs_{0.05}(FA_{0.83}MA_{0.17})_{0.95}Pb(I_{0.83}Br_{0.17})_3]$ films. The process control which was conducted involved initial experiments of subjecting the triple cation films to room temperature and % relative humidity in order to note the change in optical absorption of these films at the two water peaks (1450 nm and 1900 nm). As a step to engineer a more robust solution, the

in-situ humidity chamber was designed, allowing for a greater level of process control and repeatable measurements. The results will be presented in a similar manner, walking through the design of experiments and engineering solutions which has led to a greater understanding of the process whilst identifying the possible sources of error. This would help researchers to understand water-perovskite interaction and design experiments to exact the required results.

3.4.1 Spectral absorbance measurements

SWIR reflectance measurements are carried out on the triple cation perovskite film (dimensions: 25 mm x 20 mm). These films either have gold standard reflectance layer or mirror as a reflective layer for the laser to be used in a reflectance-based spectroscopy. Each of the samples were subjected to reflectance measurement under different exposure time, moisture content, temperature and encapsulation pattern. The films are prepared inside a glovebox, under an inert N_2 atmosphere with 0 ppm of moisture and < 2 ppm of O_2. Upon completion of fabrication, the films were stored either in the glovebox or inside a dry box (with desiccant). The films are transported to testing facility inside a sealed bag filled with desiccant crystals and taken out and subjected to the set %RH for testing.

Reflectance measurement was carried out on a Perkin Elmer Lambda 1050 spectrophotometer using 150 mm Spectralon integrating sphere and a Spectralon reflectance standard [35]. The samples were placed directly on the stage or inside the sample chamber (of the in-situ setup) and placed directly under the incident laser at a slight angle (~7°). Humidity conditions to which the films are exposed vary from 8.5 %RH to 60 %RH. The samples were heated upto 60°C for some of the tests carried out. The sample placement and alignment in the in-situ chamber setup, shown in fig 3.6, is used for testing in WaRD.

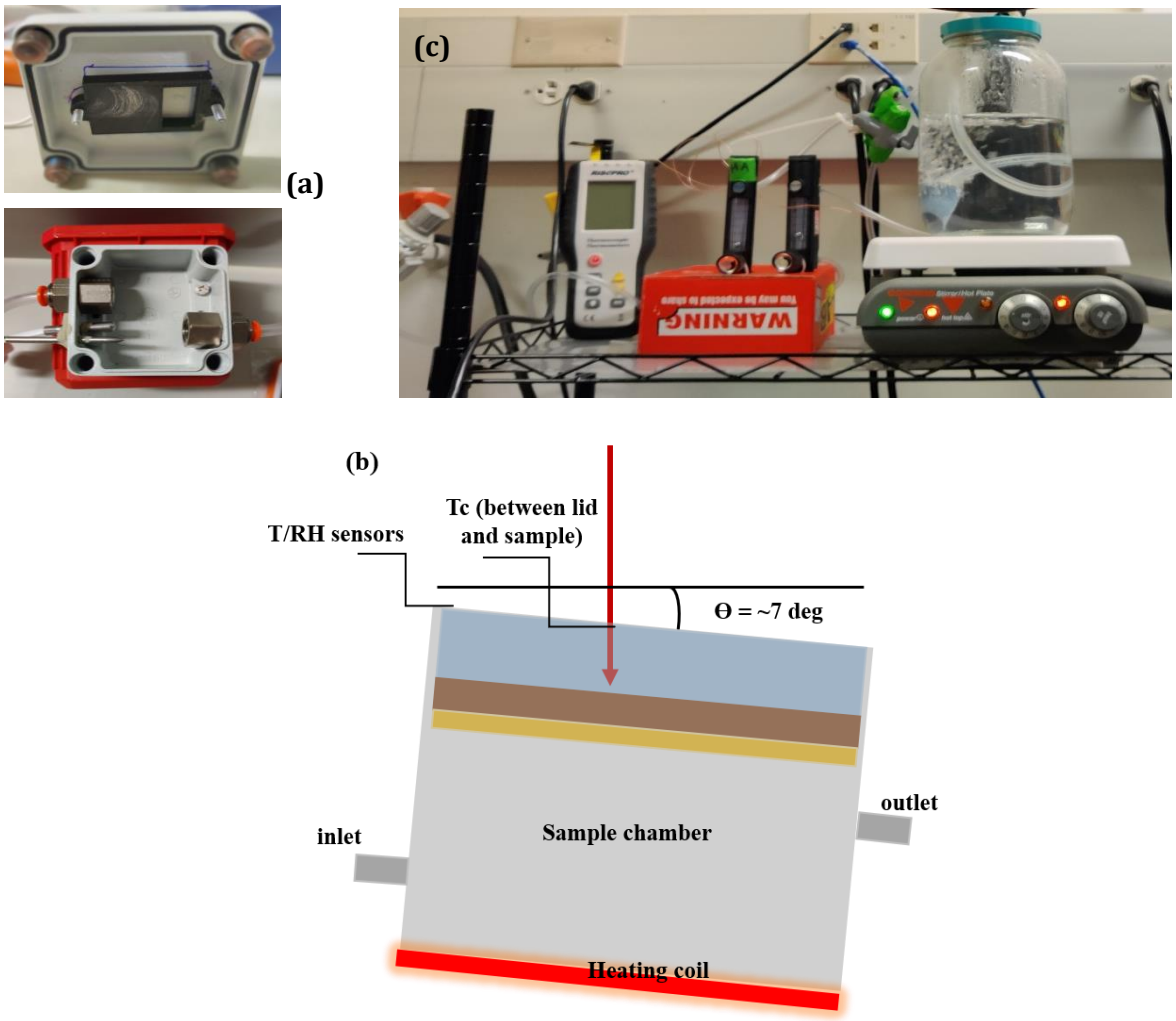

Figure 3.6: (a) Design of RH chamber with holder (b) Alignment of chamber over heating coil (c) in-situ chamber setup

3.4.2 Data collection and analysis procedure

SWIR reflectance measurements are carried out in the wavelength range from 1400 nm to 2000 nm. The IR tunable laser is the incident energy source used for spectroscopy. The voltage values are obtained through data acquisition and then normalized to give the reflectance values. These raw readings are converted to absorbance values using Beer's law and Absorbance values are plotted against the wavelength range of the scan. The thickness of the perovskite film was taken to be ~600nm, which is a laboratory standard obtained through the spin coating process. This

was later confirmed through an ellipsometry fitting. The Δ Absorbance versus wavelength plots are obtained by subtracting the values of the first scan from corresponding values of each subsequent scan. At each variable manipulation point, multiple scans were performed, and the averaged values were plotted against the wavelength range. During each scan, the laser dwell time was 0.5 seconds/wavelength, translating to a scan time of 190 seconds for 1400 – 200 nm. All analysis was performed on Python.

CHAPTER 4: Results and Discussion

4.1 WaRD spectroscopy data and tightening process controls

From the initial iteration of the experiment till the latest, the challenge of detection of the presence of moisture is systematically addressed by a series of process control. The experiments carried out include -

- Proof of concept testing
- Using in-situ RH chamber setup (Stack: Glass/Triple Cation Perovskite/Mirror)
- Using in-situ RH chamber setup (Stack: Glass/Triple Cation Perovskite/Au)
- Limit of Detection and Quantification
- Reversibility test

4.1.1 Proof of concept testing

PIB encapsulation on all sides of the sample with one exposed side to control the diffusion to occur from that edge. The sample is subject to variations in temperature and relative humidity in the room overnight (for a duration of 17.5 hours). For a given temperature and relative humidity, the absolute water content can be calculated based on the empirical formula [38]

$$Absolute\ Humidity\ \left(\frac{grams}{m^3}\right) = \frac{6.112 \text{ x } e^{\left[\frac{17.67 \text{ x } T}{T+243.5}\right]} \text{ x } rh \text{ x } 2.1674}{273.15 + T}$$

Figure 4.1 (b) shows the change in absorbance (Δ A) measured by the difference between the first and the subsequent scans at 2 of the water's spectroscopic signatures - 1450 nm (1452nm) and 1902 nm. There would be a slight shift in the position of the peak which typically occurs

during measurement. The top two subplots are the changes in absorbance values which seem to fluctuate proportionally with the slightest of change in the absolute water content in the atmosphere of measurement, stating that there is an uptake of water which occurs in a perovskite film that can be detected through WaRD spectroscopy successfully.

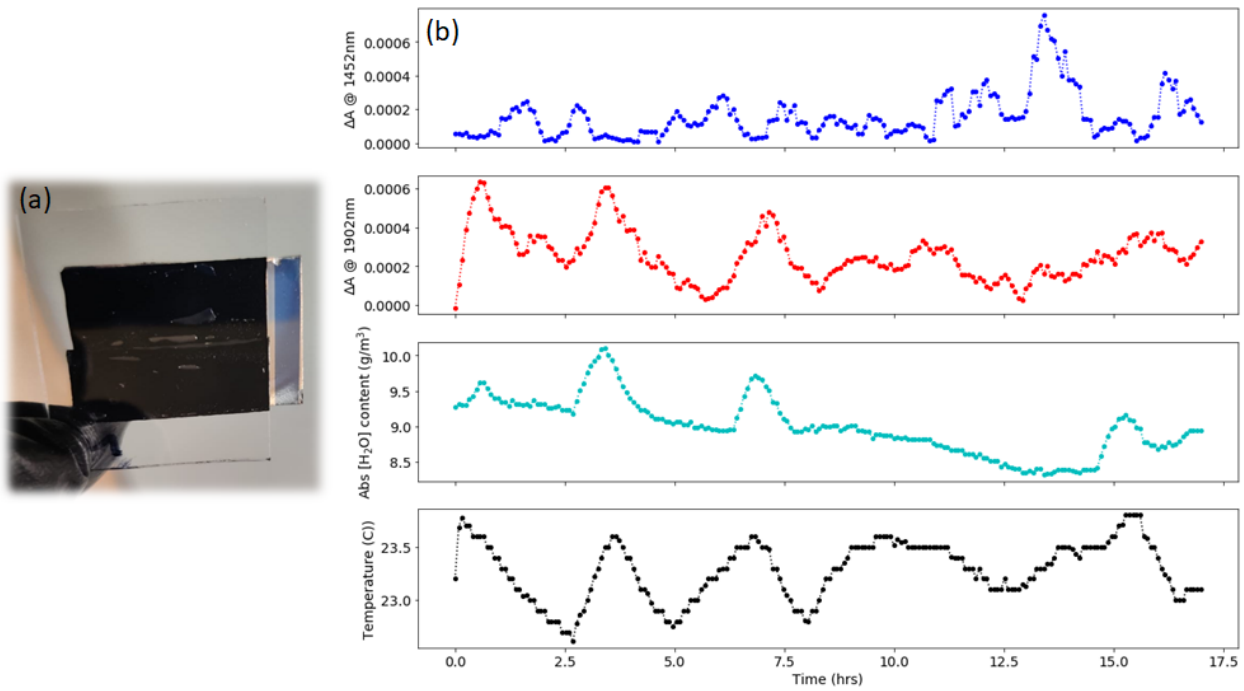

Figure 4.1: (a) Encapsulated sample with edge opening (b) Subplots (top → bottom): Δ Abs values across 17.5 hours for 1452 nm water peak, Δ Abs values across 17.5 hours for 1902 nm water peak, change in absolute [H_2O] concentration in (g/m^3), fluctuations in temperature (℃) over the scan duration.

Proof of concept established the correlation between water ingress and the absolute concentration of H_2O. Further study on this water-perovskite interaction warrants tighter conditions - effect on changing the [H_2O] of the film and effect on changing the temperature. This experiment narrowed down the stronger of the two variables with higher sensitivity to the moisture uptake content - the change in absolute water concentration, caused as a result of change in relative humidity. To examine this closer, the in-situ RH chamber was built and used for further testing.

4.1.2 Using in-situ RH chamber setup (Stack: Glass/Perovskite/Mirror)

The triple cation perovskite film is subjected to different %RH inside a sealed chamber, under ambient room temperature. The amount of relative humidity is increased inside the chamber while performing an in-situ WaRD measurement. The range of %RH is from 8.7 %RH ("dry") to 48 %RH ("humid"). Figure 4.3 shows the change in absorbance measured at a single point on the film over the duration of change in moisture content exposed. This reading is taken across the near-IR scan wavelengths of 1400 nm to 2000 nm. From the figure (Fig. 4.3), a clear change in absorbance (noted by the shift in curve) can be observed in moisture's spectroscopic signature window between 1890 nm to 1920 nm. The colors dark → light represent an increasing %RH inside the chamber: 8.7 %RH, 16 %RH, 38 %RH and 48 %RH.

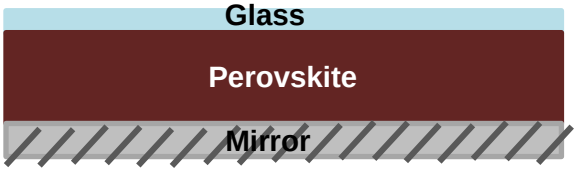

Fig 4.2 Schematic of the film used

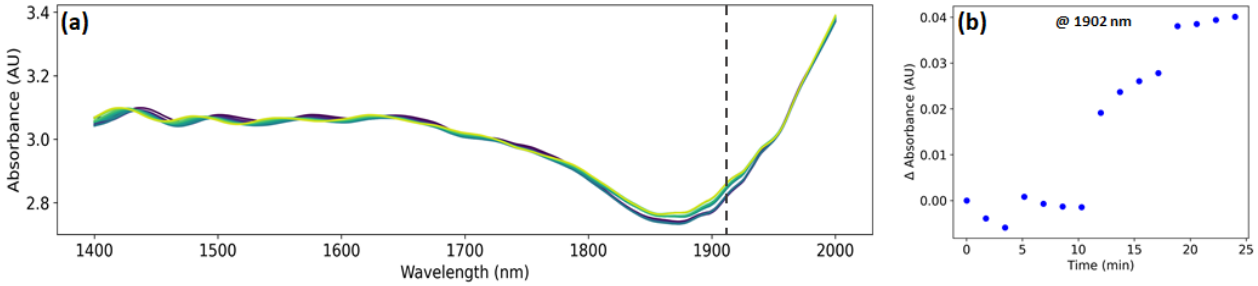

Figure 4.3: (a) Absorption spectra at different %RH and (b) the uptake (change in absorbance) at the water's signature of 1902 nm observed over a course of 25 minutes

This experiment is the first pass at measurements carried out using the in-situ chamber and a proof of tight process controls, giving reproducible results. Due to the presence of an additional reflective surface of mirror, which introduces a combination of coherent and incoherent reflections as we trace the path of light, the obtained spectra see a thin film interference pattern caused by the

triple cation perovskite. For ease of modeling the interference pattern, the stack of Glass/Perovskite/Au is chosen where the reflective mirror surface is replaced with a reflective gold layer.

4.1.3 Using in-situ RH chamber setup (Stack: Glass/Perovskite/Au)

The samples are placed in a tilted chamber setup (fig 3.6) and tested at 4 different temperatures - 30℃, 40℃, 50℃ and 60℃. At each of the conditions, a single sample is subjected to an increasing %RH inside of the chamber - 10%, 25%, 40% and 60%. For figures 4.4 - 4.7 there appears to be a "window" between 1800 nm - 1950 nm where the absorbance of water can be noted with an increase in absolute concentration of water. As the temperature is increased, there is a divergence in the absorbance curves due to either changes in film properties such as refractive index, film thickness and structure or due to a change in temperature. At 50℃ iso temperature plot, the 1450 nm peak starts showing up more prominently while the 1902 nm peak becomes much broader.

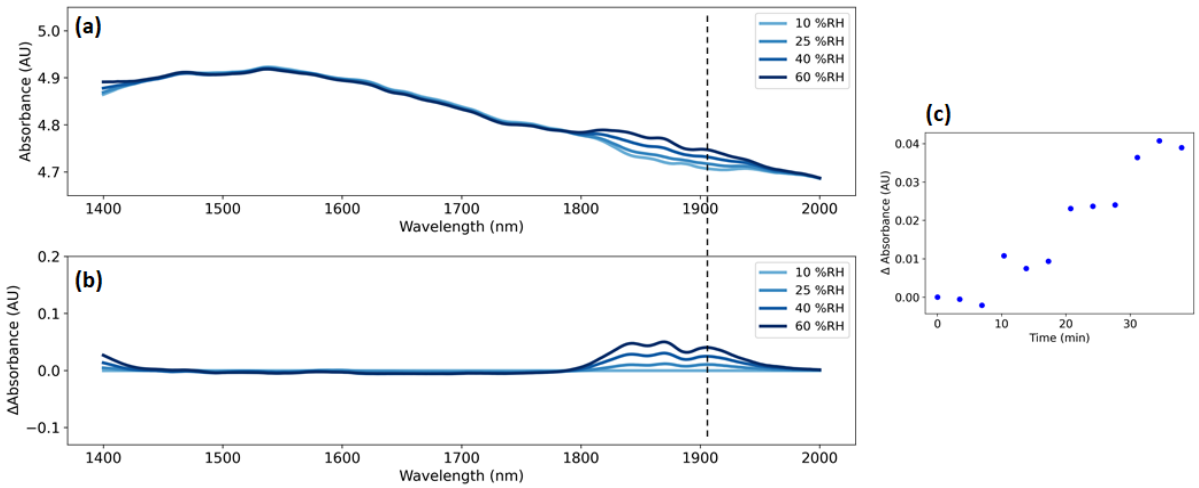

Figure 4.4: (a) Absorption spectra at 30℃ under increasing [H_2O] indicated from light blue → dark blue (b) Relative change in absorption at each %RH (c) "Uptake"/increase in absorbance at peak (1902 nm) with increase in water exposure with increasing time.

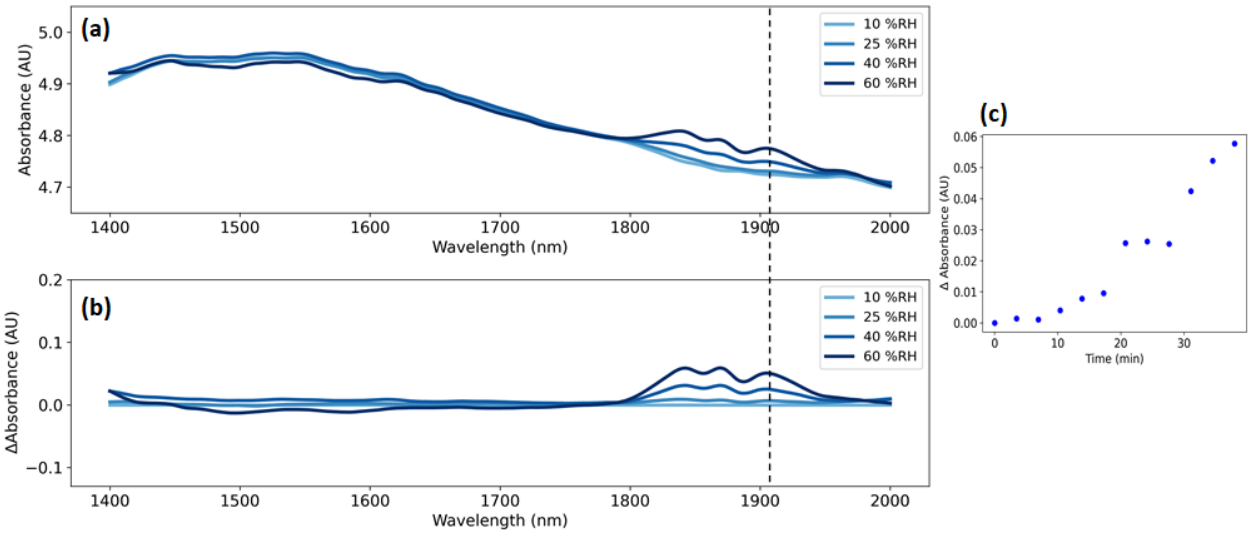

Figure 4.5: (a) Absorption spectra at 40°C under increasing [H_2O] indicated from light blue → dark blue (b) Relative change in absorption at each %RH (c) "Uptake"/increase in absorbance at peak (1902 nm) with increase in water exposure with increasing time.

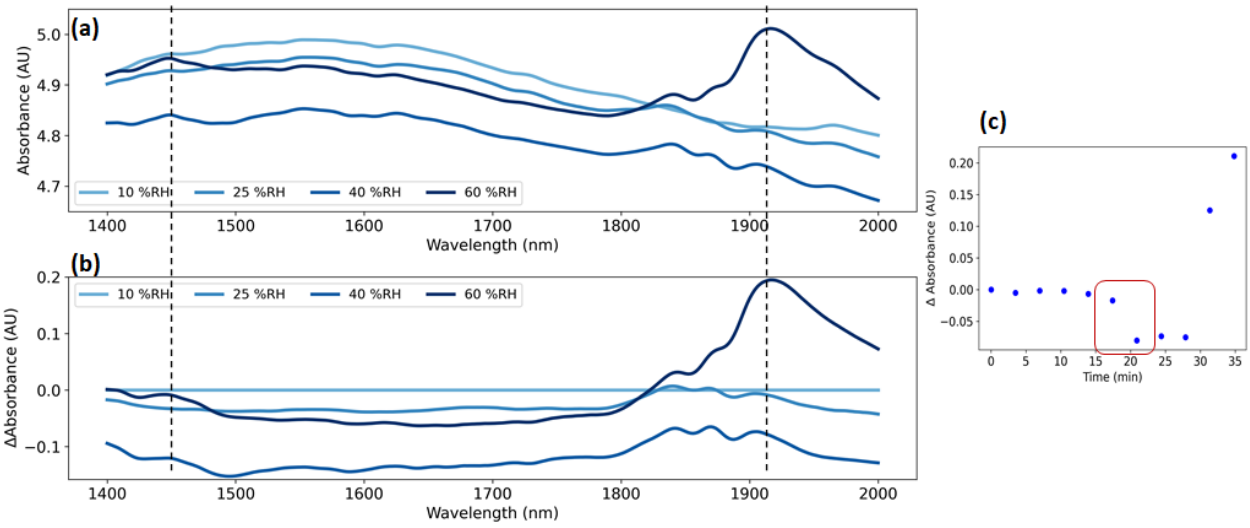

Figure 4.6: (a) Absorption spectra at 50°C under increasing [H_2O] indicated from light blue → dark blue (b) Relative change in absorption at each %RH (c) "Uptake"/increase in absorbance at peak (1902 nm) with increase in water exposure with increasing time.

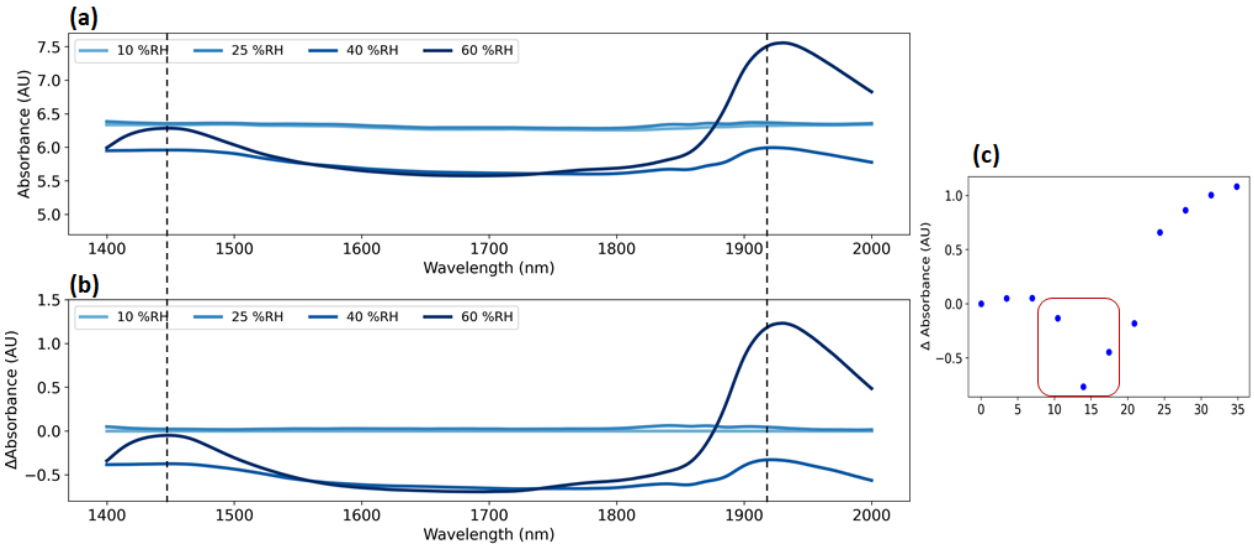

Figure 4.7: (a) Absorption spectra at 60°C under increasing [H_2O] indicated from light blue → dark blue (b) Relative change in absorption at each %RH (c) "Uptake"/increase in absorbance at peak (1902 nm) with increase in water exposure with increasing time.

4.1.4 Background removal and peak isolation

Figures 4.4 – 4.7 are each offset due to background noise which gets manifested into the signal that we observe. Fitting a baseline and removing the background helps isolate just the peaks that we observe in the spectrum by removing the tilt. The background removal is done by approximating a baseline to the given spectrum by iterative Savitsky-Golay smoothing with an increasing window size to fit the spectrum accurately. The baseline is not allowed to rise above the actual spectrum values at any point, which helps preserve most of the signal post fitting. The function returns the spectrum with removed baseline and the baseline itself. Figure 4.8 shows a part of the process of baseline removal. The blue curve is a given spectrum prior to fitting. The orange curve represents the baseline which is fit to the spectrum iteratively. The final spectrum post fitting consists of all the iterated baselines subtracted from the original spectrum, chopping the required peaks. The figure 4.8 represents 2 such iterative window and is supposed to present a general idea of the process.

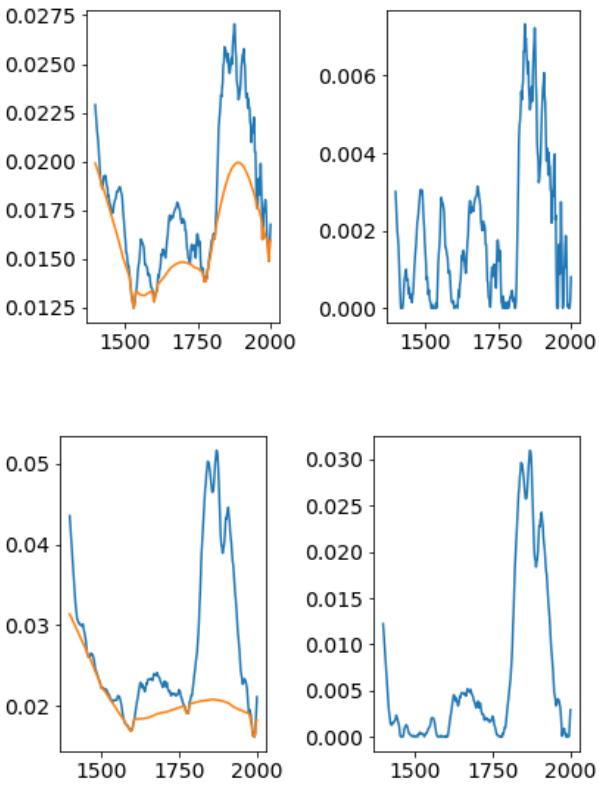

Figure 4.8 Two windows showing the process of background subtraction and peak extraction

Figure 4.9 gives the full spectrum of the iso-temperature plots after fitting. The validation of the fitting can be claimed on comparison of the peak heights obtained from Figure 4.4 and Figure 4.9 (a) for the 30°C condition and from Figures 4.5 and 4.9 (b) respectively for 40°C. The values are shown in Table 4.1.

Table 4.1 Validation of baseline fitting

% RH (30°C)	ΔAbs_original (AU)	Abs_fit (AU)
25 %	0.01000	0.0097
40 %	0.02448	0.0242
60 %	0.03958	0.0388
Max error:	- **1.97%** (overfit)	

% RH (40°C)	ΔAbs_original (AU)	Abs_fit (AU)
25 %	0.0033	0.0022
40 %	0.0243	0.0189
60 %	0.0499	0.0476
Max error:	- **22.2%** (overfit)	

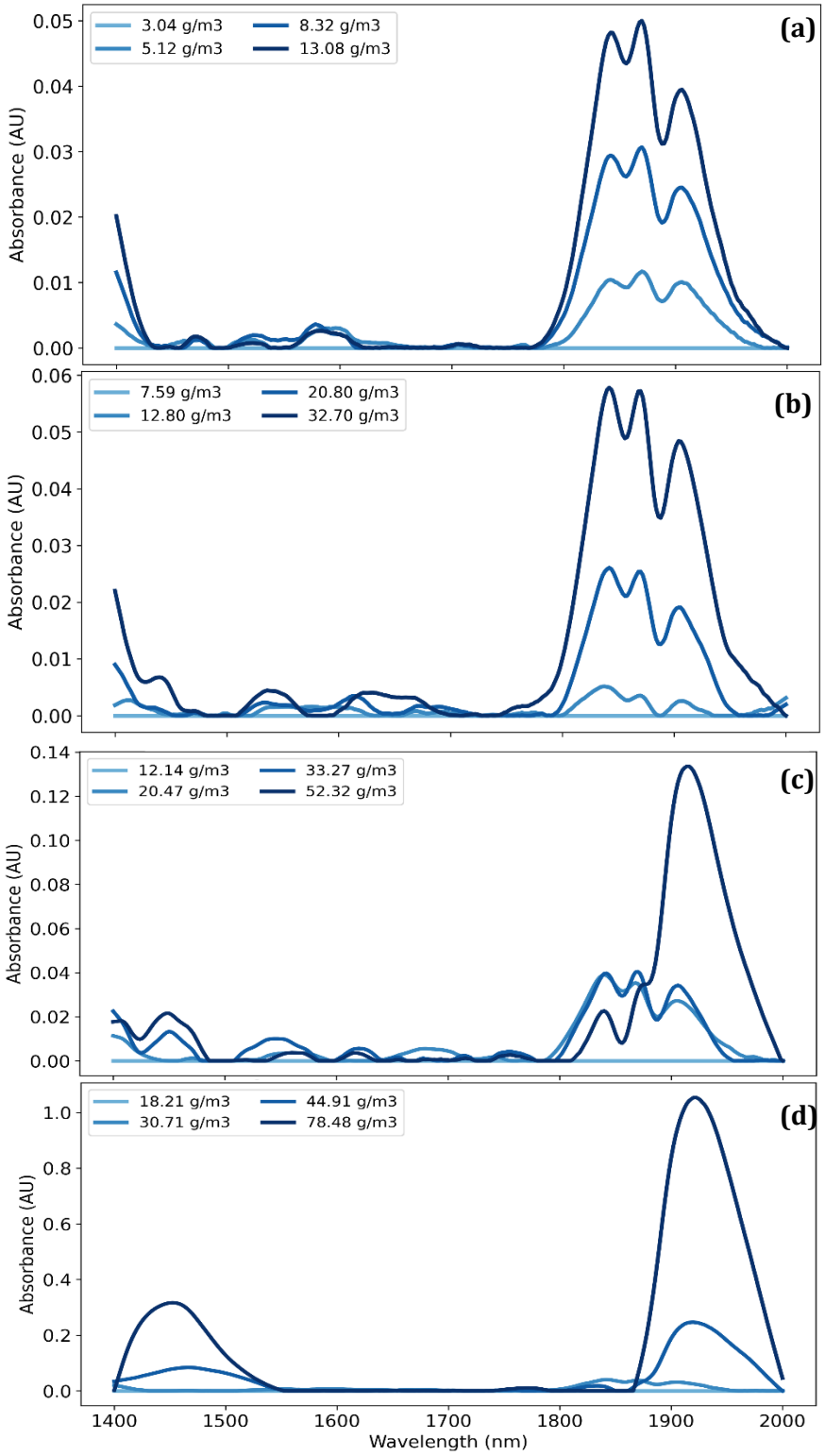

Figure 4.9: Background removal and peak isolation spectra post fitting for (a) 30℃ (b) 40℃ (c) 50℃ (d) 60℃

The values of Δ Absorbance obtained from the original spectrum is of similar magnitude as the absorbance value we obtain from the fitting which corresponds to the peak height after background is removed. The maximum error in validation of fit for the 30℃ sample is 1.97% and shows a slight overfit while the maximum error in validation for the 40℃ sample is 22.2% overfit. For the 50℃ and 60℃ samples, the original spectrum consisted of a variety of broadband compositional changes in the spectrum which caused the absorbance to have negative value (spectroscopically insignificant). Fitting of those spectrum has resulted in successful elimination of the noise in the original spectrum.

4.1.5 Calculating [H_2O] in triple cation perovskite film

For the absorption measurement for the triple cation perovskite stack at 30℃, for a given amount of absorbance change, the concentration of water which caused the said change can be calculated based on beer-lambert law :

$$A = \varepsilon * c_{H_2O} * l_{path}$$

The specific absorption coefficient for pure water (at 1920 nm) is 124 $cm^{-1}/g\ cm^{-3}$ [40] which can be converted to molar coefficient of absorption (ε_{H_2O}= *2.234*$cm^{-1}/mol\ L^{-1}$) and used in the equation to calculate the concentration of water in the film. A single unit cell of perovskite has a lattice constant of 6.278 Å [41] with which calculation of H_2O : Perovskite is done. All values are tabulated in Table 4.2 for triple cation films.

Table 4.2 Calculated concentration of water in films across varying T and RH

Temperature	[H_2O] in chamber	Absorbance_fit (AU)	[H_2O] in film (M)	H_2O : Perovskite
30°C (3.04 g/m^3 reference)	5.12 g/m^3	0.0098297	36.69	5.46
	8.32 g/m^3	0.0242699	90.61	13.50
	13.08 g/m^3	0.038869	145.12	21.63
40°C (7.59 g/m^3 reference)	12.80 g/m^3	0.0022959	8.57	1.27
	20.80 g/m^3	0.0188824	70.49	10.50
	32.70 g/m^3	0.0476298	177.82	26.50
50°C (12.14 g/m^3 reference)	20.47 g/m^3	0.0269101	100.47	14.97
	33.27 g/m^3	0.0331816	123.88	18.46
	52.32 g/m^3	0.115734	432.10	64.41
60°C (18.21 g/m^3 reference)	30.71 g/m^3	0.0307125	114.66	17.09
	44.91 g/m^3	0.20065	749.14	111.67
	78.48 g/m^3	0.879067	3282.06	489.25

These experiments and calculations indicate the presence of large quantities of water inside the perovskite films which are indicative of degradation, yet visual inspection post measurement maintains the dark brown color of the film, thereby pointing to the intactness of the film's properties. The maximum theoretical limit when it comes to water: perovskite ratio is 2:1, which would lead to a complete degradation to lead iodide and result in the film turning yellow. Even a 1:1 water: perovskite ratio is indicative of high-water content. Table 4.3 gives the theoretical molar concentration of water in the films which would result in a molar ratio from 0.001 to 1.

Table 4.3 Theoretical water concentration to produce molar ratios from 0.001 – 1

Molar ratio	0.001	0.1	0.2	0.3	0.4	0.5	0.6	0.7	0.8	0.9	1
[H_2O] in film (M)	0.006	0.670	1.341	2.012	2.682	3.353	4.024	4.695	5.365	6.036	6.707

The contradicting result prompts the need to conduct control tests in order to identify the sources of error in the detection of the presence of water which could contribute to this measurement of excess water.

4.2 Control tests to identify sources of excess water presence

The measurement of Glass/Perovskite/Au stack was carried out on an unencapsulated film which could be potentially a source of error which could cause the presence of excess water since the diffusion is not occurring in a controlled manner. Yet, the math suggests that there is more than one such source which is causing the inflated value. Some of the possible sources of error in this experiment could be:

- Measurement of water peaks (interfacial water) in the gold substrate
- Measurement of water peaks from behind the sample (due to pinholes and other defects)
- Measurement of water in the optical path from the laser to sample

4.2.1 WaRD on gold substrate

An 80 nm thick layer of gold is thermally evaporated onto a clean glass substrate and is placed in the sample chamber under exact same conditions as that of a perovskite film (30°C and across %RH from 10% to 60%). Scans from 1400 nm - 2000 nm show the presence of water peaks in the window between 1800 nm to 1950 nm in the gold sample as well. This could indicate the presence of interfacial water which also contributes to the measurement.

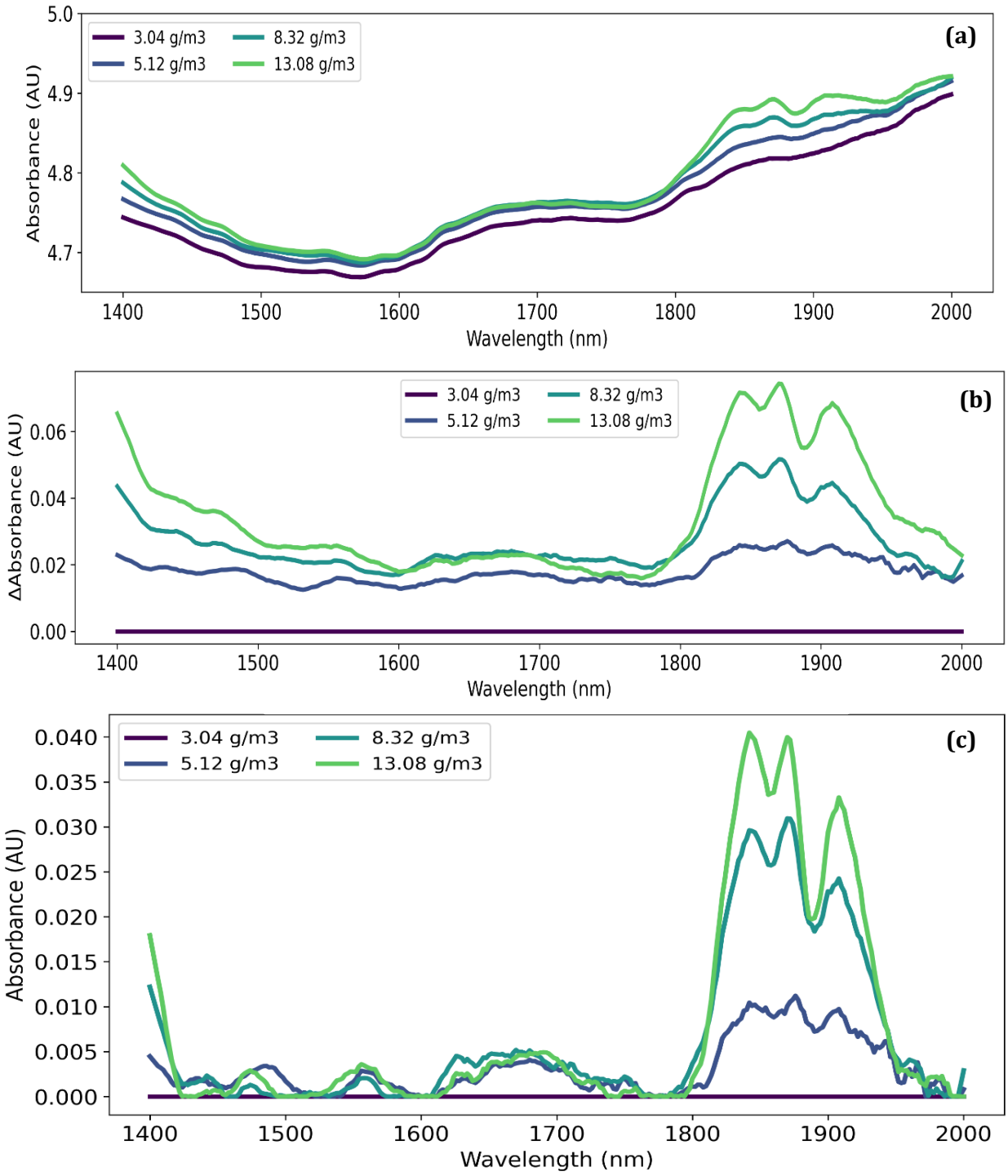

Figure 4.10: (a) Absorption spectra of Glass/Au with increasing %RH (b) Relative change in absorbance of Glass/Au under the same %RH conditions (c) Background removal and peak isolation spectrum of (a)

4.2.2 Recalculated [H_2O] in film accounting for interfacial water

The control test carried out indicated water peaks (1800nm – 1950nm) in an unencapsulated Glass/Au film. Similar background removal and peak extraction is performed on the raw spectrum and the change in concentration of water in the triple cation perovskite film across %RH at 30℃ is recalculated and the values are tabulated in Table 4.4.

Table 4.4 Re-calculating concentration water in film across different %RH at 30℃

Temp	[H_2O] in chamber	Abs_total (AU)	Abs_control (AU)	|Abs_film| (AU)	[H_2O] in film (M)	H_2O : Perovskite
30℃ (3.04 g/m^3 reference)	5.12 g/m^3	0.0098297	0.009175	6.547e-4	2.444	0.36
	8.32 g/m^3	0.0242699	0.022702	1.567e-3	5.850	0.87
	13.08 g/m^3	0.0388695	0.030635	8.2345e-3	30.744	4.58

4.2.3 WaRD on encapsulated sample

The encapsulation is carried out in a pattern like in Fig 3.5 (b) and (d). The optical path of the laser hits the PIB square rather than going through the pinholes of the film. In this square encapsulation, there is still edge diffusion which can occur in the film. In contrast, encapsulation is done using a PIB edge seal in addition to the square encapsulation. This is to ensure "quiet" data from within the film itself. The figure 4.11 still depicts the presence of "water" peaks observed in the window from 1800 - 1950 nm. The lowest and highest %RH values (dark → light) are positively offset, which can easily be corrected by accounting for background subtraction during calculations. Background removal and peak isolation of the peak region (1800nm – 1950nm) for the encapsulated samples are shown in figure 4.12.

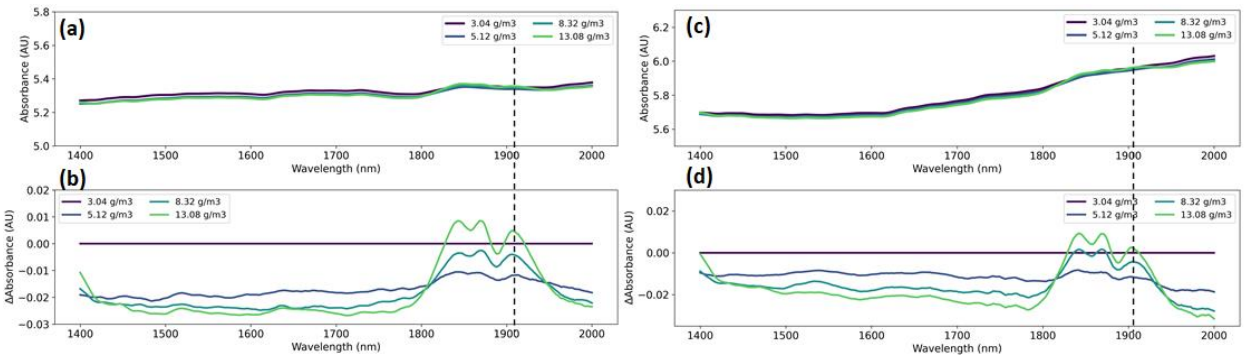

Figure 4.11: (a) & (b) Absorption and Δ Absorption spectra of square encapsulation with increasing %RH and (c) & (d) Absorption and Δ Absorption spectra of PIB edge + square encapsulation with increasing %RH

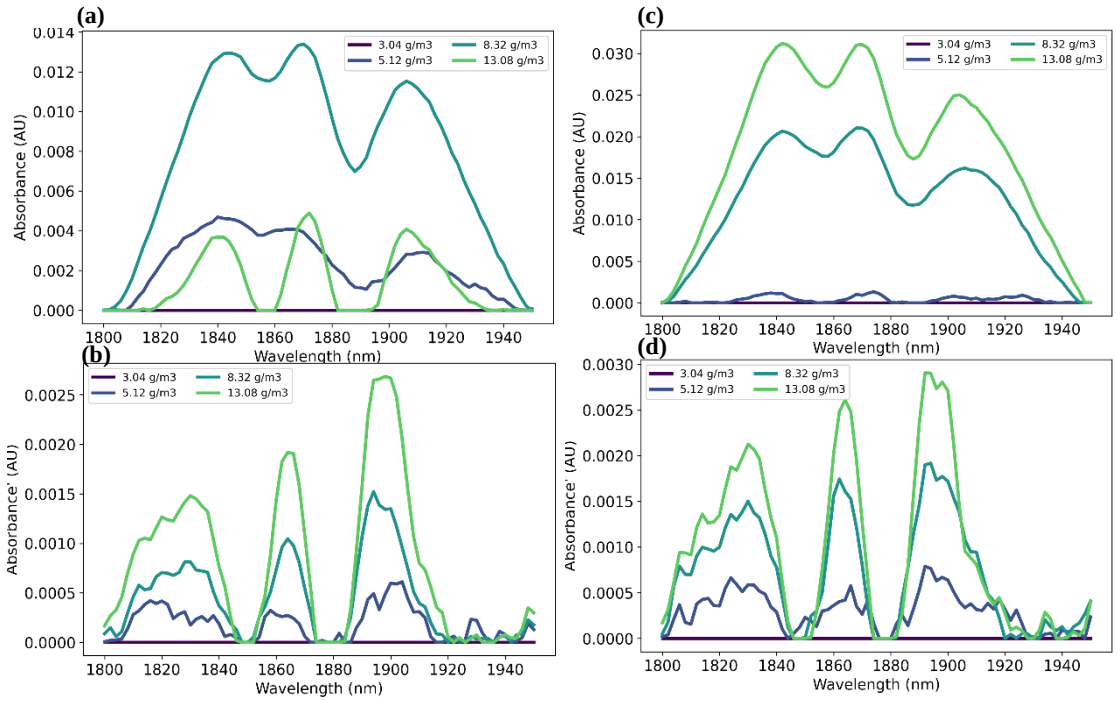

Figure 4.12: Peak isolation on encapsulated sample on (a) & (c) absorbance data (b) & (d) 1st derivative of absorbance data. (a)-(b) Square encapsulated sample and (c)-(d) Edge and square encapsulated sample

4.2.4 WaRD on sample with CDA

In order to account for the final source of error: measuring water in the optical path from the laser to the sample chamber, a compressed dry air (CDA) line is run above the sample chamber

during the measurement. A sample of edge seal + square encapsulated film is used for testing. The same conditions are used, and the graph indicates a much “quieter” distribution. The change in absorbance values is uniform (with a standard deviation of 0.005 AU) indicating that not much diffusion has occurred in the sample. This also means that the presence of excess water could be arising from the atmospheric water vapor in the testing setup which attenuates the signal before it could even reach the film. A change in the setup design to make sure there are no leaks that could occur, would be a first critical step in pursuing this project further.

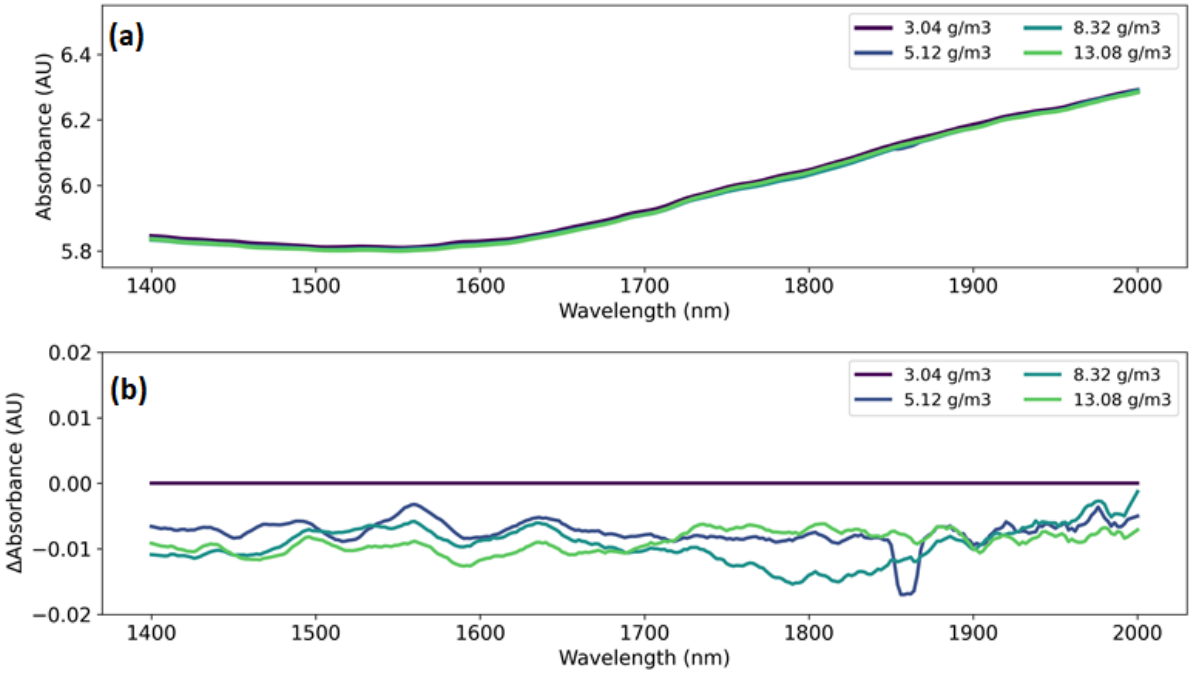

Figure 4.13: (a) Absorption spectra of CDA encapsulated film with increasing %RH and (b) Relative change in absorbance under the same %RH condition

4.3 Limit of detection and quantification

In order to establish a statistically significant detection of moisture content, limit of detection and quantification tests were carried out on a triple cation film stack

(Glass/Perovskite/Au) under 30°C at 5 different %RH values while CDA was continually pumped above the sample chamber, along the optical path. The presence of CDA caused some fluctuations in the reading. Multiple scans were carried out at a particular temperature/humidity condition and then averaged to carry out the LOD/LOQ calculations.

Limit of detection is the lowest concentration of the measurand that can be detected at a specified confidence level (CI: 95%, α = 0.05) and is given by the formula: LOD = $3.3 * \frac{S_Y}{S}$ [42,43]

Limit of quantification is the lowest concentration of the measurand that can be determined with an acceptable level of repeatability, precision and trueness. LOQ = $10 * \frac{S_Y}{S}$ [42,43]

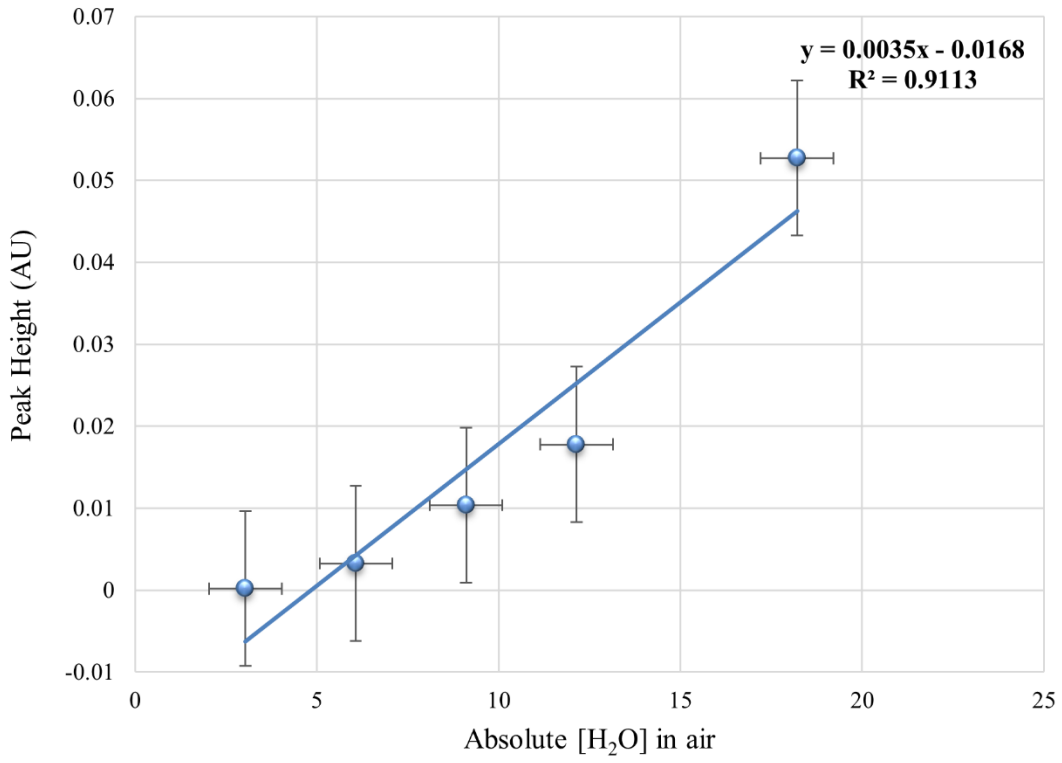

Figure 4.14: LOD/LOQ plot of obtained peak heights against the concentration of water in air for perovskite film with CDA line measured from 1800 nm - 2000nm

The extracted limit of detection from the plot is 6.94 g/m^3 and the limit of quantification is 21.03 g/m^3. The error bars are plotted and adjusted to represent one standard error in the vertical and horizontal distance to the regression line.

4.4 Test for reversibility of hydration

The hydration of perovskites is a reversible process until the point where a dihydrate intermediate is formed, causing complete conversion to PbI_2. In fig 4.15, the stack used comprises Glass/Perovskite/Au. The blue curves represent forward sweeps with increasing water content while the red curves are reverse sweeps with decreasing water content. There is water uptake observed with increasing %RH while a similar dry out with decreasing %RH. At lower [H_2O] there is a better overlap as can be seen from 15% and 25% F/R curves and at higher [H_2O] there is still some residual H_2O left in the film to allow for a perfect overlap.

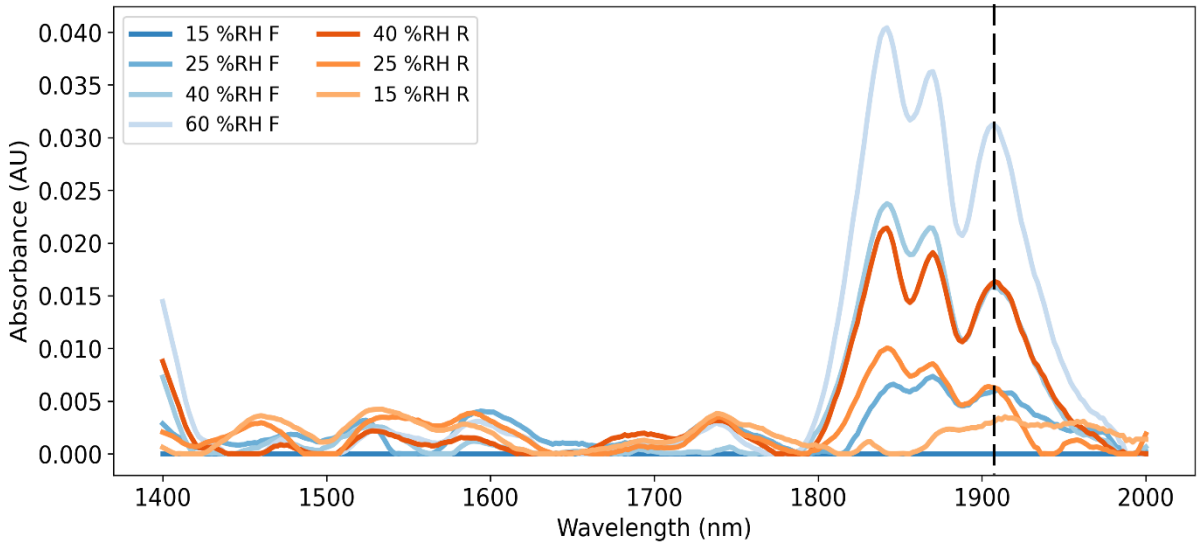

Figure 4.15: Forward and reverse sweeps indicating a reversible trend in the process of hydration

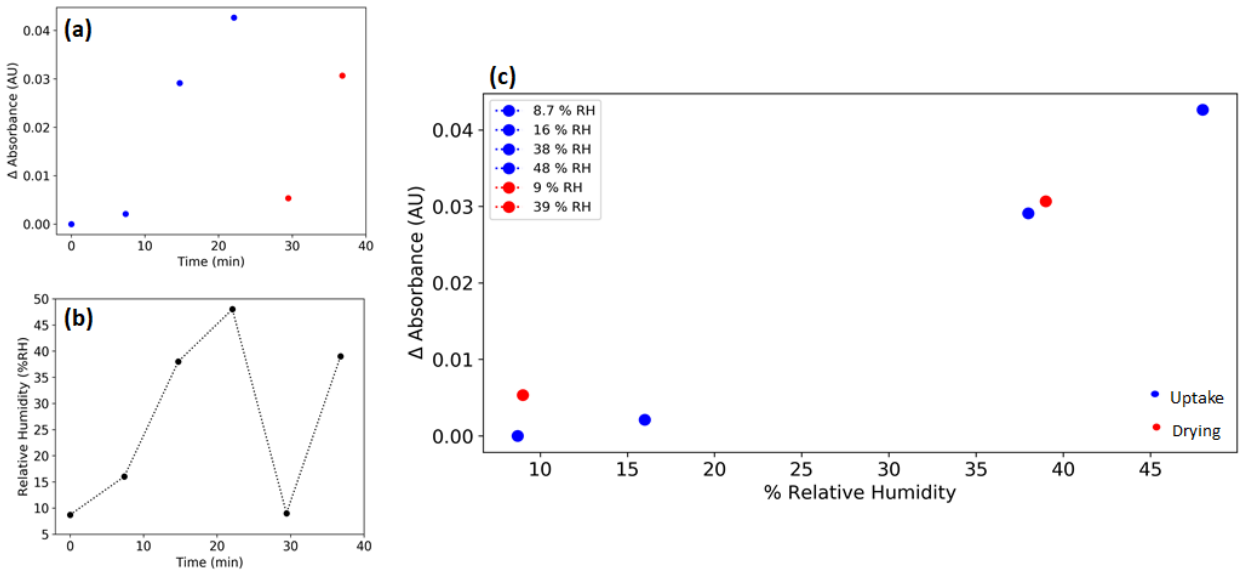

Figure 4.16: (a) Uptake and dry out in perovskite film with changing %RH measured at 1902 nm (b) change in %RH during the measurement (c) Overlay of both data

A similar test carried out on a stack of Glass/Perovskite/Mirror also indicated the reversibility in the hydration and dry outs plots. Fig 4.16 (c) shows the uptake (increase in absorbance with an increase in concentration) and the dry out (decrease in absorbance with a decrease in moisture concentration) overlays with a little bit of a hysteresis between the two, which could be due to thin film interferences which are present prominently in the mirror base samples or could be because the dry out was not 100% when the measurement was carried out indicating that uptake occurs at a quicker rate than a dry out.

CHAPTER 5: Conclusion and Future work

In conclusion, this study provides an in-situ technique to observe and study the ingress of moisture in a hybrid organic-inorganic triple cation perovskite. The absorption can be clearly discerned through the WaRD (water reflectometry detection) method, where the near-infrared measurements allow for a spectroscopic window centered around 1450 nm and between 1800 nm to 1950 nm where moisture can be detected. The uptake and dry out of moisture are noted to be proportional yet reversible interaction with perovskite chemistry (tested for values of %RH under 60%). Applying science and mathematics, we can quantify the amount of moisture that is present in our test films. Doing so has shown that WaRD is a sensitive tool which can pick up traces of moisture from the surrounding as well as from the film itself without destroying or even entirely degrading it.

Through extensive process control and creative engineering solutions, we have been able to collect high quality data to not only understand the perovskite-water interaction but also help identify sources of error which led to detection of excess water in films and with better research practices and engineering solutions, this challenge can be addressed based on collective information that can be obtained from this study. WaRD tool, which previously has been applied only to map water content in silicon modules, can be extended in its application to perovskite modules.

This study has shown the potential application and experimental control required to fine-tune the technique, but further research needs to be done in order to provide insights on the rate of

diffusion of moisture, its spatial distribution in the perovskite film and finally, its role in compositional and structural changes. In extension, researchers can use this setup to compare the interaction of water across various perovskite chemistries and address the moisture ingress in a full device stack in order to develop better encapsulation or passivation techniques in the future. By addressing one of the biggest bottlenecks (moisture-perovskite interaction) to have existed in perovskite research, the research community would be able to take the field of perovskites a huge step closer to commercialization.

REFERENCES

1) https://en.wikipedia.org/wiki/Population_growth

2) K. Jäger, “Solar Energy: Fundamentals, Technology, and Systems”. Delft University of Technology, 2014

3) www.eia.gov

4) https://ourworldindata.org/energy-production-consumption

5) Panwar, N. L., S. C. Kaushik, and Surendra Kothari. "Role of renewable energy sources in environmental protection: A review." Renewable and sustainable energy reviews 15.3 (2011): 1513-1524.

6) Bull, Stanley R. "Renewable energy today and tomorrow." Proceedings of the IEEE 89.8 (2001): 1216-1226.

7) Park, Nam-Gyu. "Perovskite solar cells: an emerging photovoltaic technology." Materials today 18.2 (2015): 65-72.

8) Green, Martin A., Anita Ho-Baillie, and Henry J. Snaith. "The emergence of perovskite solar cells." Nature photonics 8.7 (2014): 506-514.

9) https://www.nrel.gov/pv/cell-efficiency.html

10) https://www.pveducation.org/pvcdrom/solar-cell-operation/solar-cell-structure

11) Sun, Shuangyong, Teddy Salim, Nripan Mathews, Martial Duchamp, Chris Boothroyd, Guichuan Xing, Tze Chien Sum, and Yeng Ming Lam. "The origin of high efficiency in low-temperature solution-processable bilayer organometal halide hybrid solar cells." Energy & Environmental Science 7, no. 1 (2014): 399-407.

12) Yin, Wan-Jian, Tingting Shi, and Yanfa Yan. "Unique properties of halide perovskites as possible origins of the superior solar cell performance." Advanced Materials 26.27 (2014): 4653-4658.

13) Correa-Baena, J. P., Abate, A., Saliba, M., Tress, W., Jacobsson, T. J., Grätzel, M., & Hagfeldt, A. (2017). The rapid evolution of highly efficient perovskite solar cells. Energy & Environmental Science, 10(3), 710-727.

14) McGehee, Michael D. "Fast-track solar cells." Nature 501.7467 (2013): 323-325.

15) Kumar, R. E., Von Gastrow, G., Leslie, J., Meier, R., Bertoni, M. I., & Fenning, D. P. (2019). Quantitative determination of moisture content in solar modules by short-wave infrared reflectometry. IEEE Journal of Photovoltaics, 9(6), 1748-1753.

16) Davies, A. M. C. "An introduction to near infrared (NIR) spectroscopy." (2014).

17) Saliba, M., Correa-Baena, J.P., Wolff, C.M., Stolterfoht, M., Phung, N., Albrecht, S., Neher, D. and Abate, A., 2018. How to Make over 20% Efficient Perovskite Solar Cells in Regular (n–i–p) and Inverted (p–i–n) Architectures. Chemistry of Materials, 30(13), pp.4193-4201.

18) Park, N. C., W. W. Oh, and D. H. Kim. "Effect of temperature and humidity on the degradation rate of multicrystalline silicon photovoltaic module." International Journal of Photoenergy 2013 (2013).

19) Kempe, Michael D. "Modeling of rates of moisture ingress into photovoltaic modules." Solar Energy Materials and Solar Cells 90.16 (2006): 2720-2738.

20) Salado, Manuel, Lidia Contreras-Bernal, Laura Caliò, Anna Todinova, Carmen López-Santos, Shahzada Ahmad, Ana Borras, Jesús Idígoras, and Juan A. Anta. "Impact of moisture on efficiency-determining electronic processes in perovskite solar cells." Journal of Materials Chemistry A 5, no. 22 (2017): 10917-10927.

21) Galinski, E. A., Stein, M., Amendt, B., & Kinder, M. (1997). The kosmotropic(structure-forming) effect of compensatory solutes. Comparative Biochemistry and Physiology Part A: Physiology, 117(3), 357-365.

22) Stomp, M., Huisman, J., Stal, L. J., & Matthijs, H. C. (2007). Colorful niches of phototrophic microorganisms shaped by vibrations of the water molecule. The ISME journal, 1(4), 271-282.

23) http://www1.lsbu.ac.uk/water/water_vibrational_spectrum.html

24) Segtnan, V. H., Šašić, Š., Isaksson, T., & Ozaki, Y. (2001). Studies on the structure of water using two-dimensional near-infrared correlation spectroscopy and principal component analysis. Analytical chemistry, 73(13), 3153-3161.

25) Curcio, J. A., & Petty, C. C. (1951). The near infrared absorption spectrum of liquid water. JOSA, 41(5), 302-304.

26) Burneau, A. (1990). Near infrared spectroscopic study of the structures of water in proton acceptor solvents. Journal of molecular liquids, 46, 99-127.

27) Leguy, A.M., Hu, Y., Campoy-Quiles, M., Alonso, M.I., Weber, O.J., Azarhoosh, P., Van Schilfgaarde, M., Weller, M.T., Bein, T., Nelson, J. and Docampo, P., 2015. Reversible hydration of CH3NH3PbI3 in films, single crystals, and solar cells. Chemistry of Materials, 27(9), pp.3397-3407.

28) Huang, J., Tan, S., Lund, P. D., & Zhou, H. (2017). Impact of H 2 O on organic–inorganic hybrid perovskite solar cells. Energy & Environmental Science, 10(11), 2284-2311.

29) Han, Yu, Steffen Meyer, Yasmina Dkhissi, Karl Weber, Jennifer M. Pringle, Udo Bach, Leone Spiccia, and Yi-Bing Cheng. "Degradation observations of encapsulated planar CH 3 NH 3 PbI 3 perovskite solar cells at high temperatures and humidity." Journal of Materials Chemistry A 3, no. 15 (2015): 8139-8147.

30) Hall, G.N., Stuckelberger, M., Nietzold, T., Hartman, J., Park, J.S., Werner, J., Niesen, B., Cummings, M.L., Rose, V., Ballif, C. and Chan, M.K., 2017. The role of water in the reversible optoelectronic degradation of hybrid perovskites at low pressure. The Journal of Physical Chemistry C, 121(46), pp.25659-25665.

31) Li, Y., Xu, X., Wang, C., Wang, C., Xie, F., Yang, J., & Gao, Y. (2015). Degradation by exposure of coevaporated CH3NH3PbI3 thin films. The Journal of Physical Chemistry C, 119(42), 23996-24002.

32) Ledinský, Martin, Philipp Löper, Bjoern Niesen, Jakub Holovský, Soo-Jin Moon, Jun-Ho Yum, Stefaan De Wolf, Antonín Fejfar, and Christophe Ballif. "Raman spectroscopy of organic–inorganic halide perovskites." The journal of physical chemistry letters 6, no. 3 (2015): 401-406.

33) Kakekhani, A., Katti, R. N., & Rappe, A. M. (2019). Water in hybrid perovskites: Bulk MAPbI3 degradation via super-hydrous state. APL Materials, 7(4), 041112.

34) Yang, J., Siempelkamp, B. D., Liu, D., & Kelly, T. L. (2015). Investigation of CH3NH3PbI3 degradation rates and mechanisms in controlled humidity environments using in situ techniques. ACS nano, 9(2), 1955-1963.

35) Kumar, R. E., Von Gastrow, G., Leslie, J., Meier, R., Bertoni, M. I., & Fenning, D. P. (2019). Quantitative determination of moisture content in solar modules by short-wave infrared reflectometry. IEEE Journal of Photovoltaics, 9(6), 1748-1753.

36) Hepp, Johannes, Andreas Vetter, Stefan Langner, Michael Woiton, Gordana Jovicic, Klaus Burlafinger, Jens A. Hauch, Christian Camus, Hans-Joachim Egelhaaf, and Christoph J. Brabec. "Infrared absorption imaging of water ingress into the encapsulation of (opto-) electronic devices." IEEE Journal of Photovoltaics 9, no. 1 (2018): 252-258.

37) Zhang, W., Xiong, J., Li, J., & Daoud, W. A. (2019). Mechanism of water effect on enhancing the photovoltaic performance of triple-cation hybrid perovskite solar cells. ACS applied materials & interfaces, 11(13), 12699-12708.

38) https://carnotcycle.wordpress.com/2012/08/04/how-to-convert-relative-humidity-to-absolute-humidity/

39) https://www.engineeringtoolbox.com/salt-humidity-d_1887.html#:~:text=Saturated%20salt%2Fwater%20solutions%20can,used%20to%20calibrate%20humidity%20sensors.

40) Palmer, K. F., & Williams, D. (1974). Optical properties of water in the near infrared. JOSA, 64(8), 1107-1110.

41) Correa-Baena, J.P., Luo, Y., Brenner, T.M., Snaider, J., Sun, S., Li, X., Jensen, M.A., Hartono, N.T.P., Nienhaus, L., Wieghold, S. and Poindexter, J.R., 2019. Homogenized halides and alkali cation segregation in alloyed organic-inorganic perovskites. Science, 363(6427), pp.627-631.

42) https://www.eflm.eu/files/efcc/Zagreb-Theodorsson_2.pdf

43) https://arts-sciences.und.edu/academics/chemistry/kubatova-research-group/_files/docs/determination_of_lods_new.pdf